24 Hills Road, **P** 01223 855346
Cambridge **W** elifesciences.org
CB2 1JP **T** @elife_sciences

FOR PEER REVIEW - CONFIDENTIAL

A multilayer circuit architecture for the generation of distinct locomotor behaviors in Drosophila

Tracking no: 10-09-2019-RA-eLife-51781

Impact statement: Generation of a premotor/motor neuron comprehensive TEM reconstruction, functional optogenetics, and recurrent network modeling reveals different phase relationships among a subset of Drosophila motor neurons in forward versus backward locomotion.

Competing interests: No competing interests declared

Author contributions:
Chris Doe: Conceptualization; Data curation; Supervision; Funding acquisition; Investigation; Methodology; Writing—original draft; Project administration; Writing—review and editing Brandon Mark: Conceptualization; Resources; Data curation; Software; Formal analysis; Validation; Investigation; Visualization; Methodology; Writing—original draft; Writing—review and editing Aref Zarin: Data curation; Formal analysis; Validation; Investigation; Methodology; Writing—original draft; Writing—review and editing Albert Cardona: Resources; Software; Funding acquisition; Methodology; Writing—original draft; Writing—review and editing Ashok Litwin-Kumar: Conceptualization; Resources; Software; Funding acquisition; Validation; Methodology; Writing—original draft; Writing—review and editing

Funding:
HHMI: Chris Q Doe, Aref Arzan Zarin, Albert Cardona, n/a; NIH: Chris Q Doe, Brandon Mark, HD27056 The funders had no role in study design, data collection and interpretation, or the decision to submit the work for publication.

Data Availability:
All data generated or analysed during this study are included in the manuscript and supporting files. Source data files have been provided in Supplemental Files 1 and 2.
N/A

Ethics:
Human Subjects: No Animal Subjects: No

Information for reviewers (full submissions):

eLife aims to publish work of the highest scientific standards and importance in all areas of the life and biomedical sciences, from the most basic and theoretical work through to translational, applied and clinical research. Articles must be methodologically and scientifically rigorous, ethically conducted, and objectively presented according to the appropriate community standards.

You will be asked for a general assessment and a summary of any major concerns (ideally in fewer than 500 words), as well as a list of any minor comments (optional). You will also have the opportunity to comment on the statistical rigour of the work (optional).

In your general assessment, please articulate what is exciting and whether the work represents a significant contribution. Please note our guidelines about requests for additional work:

1. We will only request new work, such as experiments, analyses, or data collection, if the new data are essential to support the major conclusions. The authors must be able to do any new work in a reasonable time frame (additional work should be conducted and written up within two months); otherwise, we will usually reject the manuscript.
2. Any requests for new work must fall within the scope of the current submission and the technical expertise of the authors.

Our goal is to make peer review constructive and collaborative: after the reviews have been submitted independently, there is an online discussion between the reviewers in which each reviewer will see the identity of the other reviewers.

A multilayer circuit architecture for the generation of distinct locomotor behaviors in *Drosophila*

Aref Arzan Zarin[1,4#*], Brandon Mark[1#], Albert Cardona[2], Ashok Litwin-Kumar[3], and Chris Q. Doe[1*]

[1]Institute of Neuroscience, Institute of Molecular Biology, Howard Hughes Medical Institute, University of Oregon, Eugene, OR 97403

[2]Janelia Research Campus, Howard Hughes Medical Institute, Ashburn, VA 20147

[3]Mortimer B. Zuckerman Mind Brain Behavior Institute, Department of Neuroscience, Columbia University, 3227 Broadway, New York, New York 10027 ORCID 0000-0003-2422-6576

[4] Current address: Department of Biology, Texas A&M University, College Station, TX 77840

# Authors contributed equally
* Authors for correspondence at cdoe@uoregon.edu (CQD) and azarin@bio.tamu.edu (AAZ)

Key words: larval locomotion, motor circuits, connectome, motor neuron, premotor neuron, rhythmic behavior, *Drosophila*, calcium imaging, ssTEM, recurrent network model

Abstract

Animals generate diverse motor behaviors, yet how the same motor neurons (MNs) generate distinct behaviors remains an open question. Here we characterize neural circuits generating *Drosophila* forward and backward locomotion. We show that all body wall MNs are activated during both behaviors, but a subset of MNs change recruitment timing for each behavior. To explore how these different MN phase relationships arise, we used a serial section TEM volume to reconstruct a comprehensive larval PMN-MN connectome. We identified PMN-MN connectivity clusters consistent with observed muscle recruitment patterns; performed selected functional optogenetic validation; and generated a recurrent network model that produces the observed sequence of motor activity using only PMN/MNs. We conclude that different locomotor behaviors are generated by multiple mechanisms: muscle recruitment differences, dedicated PMN/MN connectivity; asymmetric PMN/MN morphology, and behavior-specific PMN activity.

Introduction

Locomotion is a rhythmic and flexible motor behavior that enables animals to explore and interact with their environment. Birds and insects fly, fish swim, limbed animals walk and run, and soft-body invertebrates crawl. In all cases, locomotion results from coordinated activity of muscles with different biomechanical output. This precisely regulated task is mediated by neural circuits composed of motor neurons (MNs), premotor interneurons (PMNs), proprioceptors, and descending command-like neurons (Marder and Bucher 2001; Arber 2017; Arber and Costa 2018). A partial map of neurons and circuits regulating rhythmic locomotion have been made in mouse (Crone et al. 2008; Grillner and Jessell 2009; Zagoraiou et al. 2009; Dougherty et al. 2013; Goetz et al. 2015; Bikoff et al. 2016), cat (Kiehn 2006; Nishimaru and Kakizaki 2009), fish (Kimura et al. 2013; Song et al. 2016), tadpole (Roberts et al. 2008; Roberts et al. 2010), lamprey (Grillner 2003; Mullins et al. 2011), leech (Brodfuehrer and Thorogood 2001; Kristan et al. 2005; Marin-Burgin et al. 2008; Mullins et al. 2011), crayfish (Mulloney and Smarandache-Wellmann 2012; Mulloney et al. 2014), and worm (Tsalik and Hobert 2003; Wakabayashi et al. 2004; Haspel et al. 2010; Kawano et al. 2011; Piggott et al. 2011; Wen et al. 2012b; Zhen and Samuel 2015; Roberts et al. 2016). These pioneering studies have provided a wealth of information on motor circuits, but with the exception of *C. elegans* (White et al. 1986), there has been no system where all MNs and PMNs have been identified and characterized. Thus, we are missing a comprehensive picture of how an ensemble of interconnected neurons generate diverse locomotor behaviors.

We are interested in understanding how the *Drosophila* larva executes multiple behaviors, in particular forward versus backward locomotion (Carreira-Rosario et al. 2018). Are there different MNs used in each behavior? Are the same MNs used but with distinct patterns of activity determined by premotor input? A rigorous answer to these questions requires both comprehensive anatomical information – i.e. a PMN/MN connectome – and the ability to measure rhythmic neuronal activity and perform functional experiments. All of these tools are currently available in *Drosophila*, and here we use them to characterize the neuronal circuitry used to generate forward and backward locomotion.

The *Drosophila* larva is composed of 3 thoracic (T1-T3) and 9 abdominal segments (A1-A9; Figure 1A), with sensory neurons extending from the periphery into the CNS, and motor neurons extending out of the CNS to innervate body wall muscles. Most segments contain 30 bilateral body wall muscles that form "spatial muscle groups" based on common location and orientation: dorsal longitudinal (DL; includes previously described DA and some DO muscles), dorsal oblique (DO), ventral longitudinal (VL), ventral oblique (VO), ventral acute (VA) and lateral transverse (LT)(Figure 1B)(Crossley 1978; Hooper 1986; Bate 1990). Using these muscles, the larval nervous system can generate both forward and backward locomotion (reviewed in Kohsaka et al. 2017; Clark et al. 2018). Forward crawling behavior in larvae involves a peristaltic contraction wave from posterior to anterior segments; backward crawling entails a posterior propagation of the contraction wave (Crisp et al. 2008; Dixit et al. 2008; Berni et al. 2012; Gjorgjieva et al. 2013; Heckscher et al. 2015; Pulver et al. 2015; Loveless et al. 2018; Kohsaka et al. 2019) (Figure 1A).

There are ~30 bilateral pair of MNs in each segment: 26 pair of type Ib MNs with big boutons that typically innervate one muscle; two pair of type Is MNs with small boutons that innervate large groups of dorsal or ventral muscles; one or two type III insulinergic MNs innervating muscle 12; and three type II ventral unpaired median MNs that provide octopaminergic innervation to most muscles (Table 1) (Gorczyca et al. 1993; Landgraf et al. 1997; Hoang and Chiba 2001; Landgraf et al. 2003; Choi et al. 2004; Mauss et al. 2009; Koon et al. 2011; Koon and Budnik 2012; Zarin and Labrador 2017). Elegant pioneering work showed that type Ib MNs innervating muscles in the same spatial muscle group typically projected dendrites to the same region of the dorsal neuropil, creating a myotopic map (Landgraf et al. 1997; Mauss et al. 2009). Several MNs have been shown to be rhythmically active during larval locomotion (Heckscher et al. 2012; Zwart et al. 2016), but only a few of their

premotor inputs have been described (Kohsaka et al. 2014; Heckscher et al. 2015; Fushiki et al. 2016; Hasegawa et al. 2016; Zwart et al. 2016; Takagi et al. 2017; Carreira-Rosario et al. 2018; Kohsaka et al. 2019). Some excitatory PMNs are involved in initiating activity in their target MNs (Fushiki et al. 2016; Hasegawa et al. 2016; Zwart et al. 2016; Takagi et al. 2017; Carreira-Rosario et al. 2018), while some inhibitory PMNs limit the duration of MN activity (Kohsaka et al. 2014; MacNamee et al. 2016; Schneider-Mizell et al. 2016) or produce intrasegmental activity offsets (Zwart et al. 2016). Interestingly, some PMNs are active specifically during forward locomotion or backward locomotion (Kohsaka et al. 2014; Heckscher et al. 2015; Fushiki et al. 2016; Hasegawa et al. 2016; Takagi et al. 2017; Carreira-Rosario et al. 2018; Kohsaka et al. 2019). Yet a comprehensive map of the activity and connectivity of the PMN-MN-muscle network, which is essential for a full understanding of how locomotor behavior is generated, remains unknown.

Here we address the question of how the same MNs and muscles generate two distinct behaviors: forward and backward locomotion. There are multiple mechanisms that could generate different forward and backward locomotor behaviors. (1) Different muscles could be used in each behavior. (2) One or more spatial muscle group may show a different time of recruitment in each behavior. (3) One or more single MNs may show a different time of recruitment in each behavior. (4) PMNs and/or MNs could have asymmetric morphology along the anteroposterior body axis (e.g. post-synapses in one segment, pre-synapses a different segment), resulting in a different time of recruitment in each behavior. (5) One or more PMNs could be active only in forward or backward locomotion, changing the phase relationship of their target MNs. Here we use pan-muscle activity imaging, comprehensive TEM reconstruction of all MNs and well-connected PMNs, functional optogenetics, and development of a recurrent network model to sequentially test each of these hypotheses. We identify four mechanisms that act together to generate distinct forward and backward locomotor behaviors.

Results

All body wall muscles are activated during forward and backward locomotion

Forward and backward locomotor behaviors could be generated by recruiting different muscles for each behavior, or by changing the timing of muscle recruitment for each behavior. To distinguish between these mechanisms, we performed ratiometric calcium imaging to map the activation onset of each body wall muscle during forward and backward locomotion. To date only muscle contraction data have been reported, not muscle activity data, and only for five of the 30 body wall muscles (Heckscher et al. 2012; Zwart et al. 2016). Muscle contraction could occur passively due to biomechanical linkage between adjacent muscles, so it may not be a perfect substitute for directly measuring muscle activity.

We used GCaMP6f/mCherry live imaging to measure the activation time of all 30 individual body wall muscles in the abdominal segments. We expressed GCaMP6f and mCherry using the muscle line *R44H10-LexA*, which has variable expression in sparse to dense patterns of muscles. For this experiment we analyzed larvae with dense muscle expression. We imaged both forward and backward locomotion in 2nd instar larvae (a representative animal shown in Figure 2A, D). We found that an increased GCaMP6f signal correlated with muscle contraction during both forward and backward locomotion (representative examples of muscle 6 shown in Figure 2B, E). Most importantly, all imaged muscles (30 for forward and 29 for backward) showed a significant rise in GCaMP6f fluorescence during forward and backward locomotion (Figure 2C, F; Movies 1, 2). In addition, because each type Ib MN typically innervates a single muscle, we can use muscle depolarization as a proxy for the activity of its innervating MN. We conclude that all MNs and their target muscles are activated during forward and backward locomotion.

Hierarchical clustering identifies different MN/muscle recruitment patterns during forward and backward locomotion

All muscles are recruited in both forward and backward locomotion, leading to the hypothesis that forward and backward locomotion show different muscle recruitment times. To test this hypothesis, we embedded the multidimensional crawl cycle data in two-dimensional space using principal component analysis (PCA)(Lemon et al. 2015). We aligned crawl trials by finding peaks in this 2D space which corresponded to the highest contraction amplitude of the most muscles in a given crawl (Figure 3 – figure supplement 1; see Methods). Although muscle activity appeared as a continuum with the sequential recruitment of individual muscles, hierarchical clustering of the mean activity of each muscle during forward and backward crawling revealed four groups of co-active muscles for both behaviors (Figure 3B-E; summarized in Figure 3F,G; Table 2). We call these co-activated muscle groups F1-F4 for forward and B1-B4 for backward crawling. Overall, we analyzed 27 muscles during forward locomotion and 25 muscles during backward locomotion (missing muscles were too tightly packed to extract clear activity profiles) (Table 2). Analysis of forward locomotion showed that each co-activated muscle group had a characteristic pattern of activation: e.g. F1 muscles had a more variable time of onset, whereas F4 muscles had a highly coherent onset (Figure 3B,C). Furthermore, the activation time of each co-activated muscle group was more coherent than the time of their inactivation (Figure 3B-C). Notably, these co-activated muscle groups do not fully match previously identified spatial muscle groups (compare Figure 1 and 3).

We found that the largest change in recruitment time between forward and backward locomotion was in six muscles: the three muscles in the VO spatial muscle group, and muscles 2, 11, and 18 (each in a different spatial muscle group) (Figure 3F,G; Figure 3 – figure supplement 2). The VO spatial muscle group switched from late activity during forward locomotion (F3) to early activity during backward locomotion (B1), whereas the three other neurons switched from early activity during forward locomotion (F1/2) to late activity during backward locomotion (B3/4) (Figure 3A,F,G). These changes led to a complete inversion in the timing of the VO muscles and muscle 18 (Figure 3H). Other spatial muscle groups typically did not change their timing of activation; e.g. longitudinal muscles tended to be active early and transverse muscles activated late in both behaviors (Figure 3A,F,G), consistent with prior reports tracking single muscles within each group (Heckscher et al. 2012; Zwart et al. 2016). We conclude that forward and backward locomotor behaviors arise from a relatively small number of MN/muscles that show differential recruitment during each behavior. Our results raise two new questions. (1) What mechanisms produce co-active muscle groups? (2) What mechanism produce the differential timing of the VO and 2/11/18 muscles in forward and backward locomotion? Answering these questions will help determine how the same MNs and muscles can generate two different locomotor behaviors.

TEM reconstruction of all segmental motor neurons shows that co-active motor neurons have dispersed post-synaptic sites within the dorsal neuropil

There are two hypotheses for how co-active muscle groups are established. Each pool of co-active MNs could target their dendritic post-synaptic sites to a distinct neuropil locations, where they can be innervated by different PMNs. Alternatively, each pool of co-active MNs could have overlapping post-synaptic sites, which can be selectively targeted by distinct PMNs ("labeled line" synaptic specificity) or targeted by different combinations of PMNs (combinatorial code). To distinguish between these hypotheses, we identified all MNs with single synapse resolution in a comprehensive TEM connectome (Figure 4) and mapped the neuropil location of their post-synaptic sites (Figure 5). To date, only a small fraction of MNs have been reconstructed (Heckscher et al. 2015; Fushiki et al. 2016; Zwart et al. 2016; Carreira-Rosario et al. 2018). Here, we identify and reconstruct all differentiated MNs in segment A1, which can be used as a proxy for other abdominal segments. We identified all 25 pair of type Ib MNs, both pair of type Is MNs that target large muscle groups (RP2, RP5), one pair of type III MNs that target muscle 12, and the three unpaired midline octopaminergic MNs (VUMs) (Figure 4; Table 1). The

presence of yet another type Is MN has been suggested (Hoang and Chiba 2001), but we did not find it in the TEM volume; it may be late-differentiating or absent in A1. We linked all bilateral MNs in the TEM volume to their muscle target by matching the dendritic morphology in the EM reconstruction to the dendritic morphology determined experimentally (Landgraf et al. 1997; Landgraf et al. 2003; Mauss et al. 2009) (Figure 4; Figure 4 – figure supplements 1, 2; Table 1). A dataset of all MNs that can be opened in CATMAID (Saalfeld et al. 2009) is provided as Supplemental File 1. Note that the transverse nerve MN (MN25-1b) is only present in the A2-A7 segments (Hessinger et al. 2017), so we traced it in A2. Note that in subsequent analyses we did not include the neuromodulatory VUMs MNs due to relatively undifferentiated state (few post-synapses). We found that all MNs had a dense array of post-synapses on their dendritic projections, but unlike *C. elegans* (Wen et al. 2012b), we observed no pre-synaptic contacts to other MNs or interneurons (Figure 4 – figure supplements 1, 2). In conclusion, we have successfully identified and reconstructed, at single synapse-level resolution, all differentiated MNs in segment A1 of the newly hatched larval CNS. This is a pre-requisite for mapping the location of post-synaptic sites, as well as for mapping PMN-MN connectivity (below).

Previous work has shown that motor neurons innervating a single spatial muscle group target their dendrites to a similar region of the neuropil, creating a myotopic map that provides the first layer of functional organization of the motor neuropil (Landgraf et al. 2003; Mauss et al. 2009). Given our observation that co-active muscle groups do not precisely match previously reported spatial muscle groups, we first sought to confirm the existence of a myotopic organization using every motor neuron. First, we compared MNs in the left and right A1 hemisegments and observed highly similar post-synapse clustering within the neuropil volume (Pearson correlation coefficient, $r = 0.97$), which we averaged for subsequent analysis. This validated the quality and reproducibility of the MN dendritic reconstructions and highlighted the stereotypy of MN post-synaptic locations in the neuropil. To confirm and extend previous findings, we mapped post-synaptic site location in the neuropil for MNs innervating each spatial muscle group (Figure 5A). We show that MNs innervating spatial muscle groups DL, VL, VO, VA, and LT have significantly different spatial distributions in all three axes (two sample Kolmogorov-Smirnov test; $p<.05$) with the exception of the DL/VL muscle groups which showed significance only in the mediolateral and anteroposterior axes (Figure 5A). Additionally, we observe a highly ordered hierarchical relationship between the target regions of spatial muscle groups. The largest distinction between MN input fields are those of the SN and ISN nerves. Within the MNs of the ISN, there is first a dorsal/ventral segregation followed by a longitudinal/oblique segregation (Figure 5B). Thus, we confirm and extend previous reports of MN myotopic maps, but now at the level of resolution of individual synapses.

To determine if MNs innervating each co-active muscle group also have distinct post-synaptic sites in the neuropil, we mapped post-synaptic site localization for MNs targeting each co-active muscle group. We found that post-synaptic sites of MNs innervating different forward co-active muscle groups had unique neuropil localization along all axes (Figure 5C). A similar result was observed for MNs innervating backward co-active muscle groups (data not shown). Thus, MNs targeting both spatial and co-active muscle groups show segregation of post-synaptic sites within the neuropil, although not to the extent observed for MNs targeting spatial muscle groups (Figure 5B, bottom right). Our results raise the possibility of dedicated PMNs targeting neuropil domains that contain MN post-synapses linked to different co-active muscle groups, which could be a mechanism for generating different recruitment of MNs in each co-active muscle group (see below).

To examine the relationship between differential recruitment of MNs and post-synapse localization, we analyzed three MNs that have strikingly different recruitment times between forward and backward locomotion. MN2 is active in F1 and B3 groups, MN11 is active in F1 and B4 groups, and MN18 is active in F2 and B4 groups. Do these MNs have different post-synapse localization compared to the remainder of their spatial muscle group? If so, this could explain why they have such different recruitment times, compared to the other MNs in the same spatial muscle group. Interestingly, MN18 targeted it post-synapses to a neuropil domain distinct from

the other MNs in the LT spatial muscle group (Figure 5D). In contrast, MNs 2 and 11 had post-synapse localization fully embedded within the neuropil domain containing post-synapses from the DL and DO spatial muscle groups, respectively (Figure 5E, and data not shown). We conclude that differential distributions of post-synaptic inputs can explain some but not all of the observed differences between spatial muscle groups and co-active muscle groups.

TEM reconstruction of 118 premotor neurons reveals premotor neuron pools targeting each group of co-active motor neurons

Some co-active muscle groups are innervated by MNs that target their post-synaptic sites to a common region of the dorsal neuropil, whereas other co-active muscle groups are innervated by MNs with widely distributed post-synaptic sites. In either case, the co-active MNs could be targeted by PMNs dedicated to each pool of co-active MNs, similar to the case in the mammalian spinal cord (reviewed in Arber 2017; Arber and Costa 2018). To determine whether there are "labeled lines" of PMNs innervating co-active MNs – or combinatorial coding of PMN-MN connectivity – requires a comprehensive identification of all PMNs and their MN partners. Hence, we identified and reconstructed all PMNs with dense monosynaptic contacts to MNs in segment A1. This included local premotor neurons with somata in A1 as well as neurons from adjacent segments with dense connectivity to A1 MN dendrites. We identified 118 bilateral PMNs (236 total) with connectivity to A1 MNs (Supplementary Table 1; see Methods for selection criteria). PMN cell bodies were distributed throughout the segment (Figure 6A), and as expected, their pre-synaptic (output) sites were strongly enriched in the dorsal neuropil (Figure 6B; Figure 6 – supplement 1) similar to partner MN post-synaptic sites (Landgraf et al. 1997; Mauss et al. 2009). In contrast, PMN post-synaptic (input) sites were distributed throughout the neuropil (Figure 6B,C).

We observed widespread connectivity of PMNs to multiple MNs. Each PMN synapsed with an average of 7.99 MNs (Figure 6D), and each MN had an average of 32.5 input PMNs (Figure 6E). All PMNs targeted both MNs and interneurons; there were no PMNs exclusively innervating MNs (Figure 6F). The 118 bilateral PMNs make 7495 synapses on A1 MNs which account for 12.7% of PMN output and 76% of the A1 MN input (excluding A2 MN-25) (Figure 6G). In addition, most PMNs projected contralaterally, had local arbors, and had post-synaptic inputs on their more proximal processes (Figure 6H-J). The few PMNs with pre- and post-synapses co-clustered distally (Figure 6 – supplement 1, boxed) are good candidates for non-spiking interneurons that perform local computations (reviewed in Pearson 1976; Marder and Bucher 2001). Neurotransmitter expression is known for a fraction of the PMNs (Kohsaka et al. 2014; Heckscher et al. 2015; Fushiki et al. 2016; Hasegawa et al. 2016; MacNamee et al. 2016; Zwart et al. 2016; Takagi et al. 2017; Yoshino et al. 2017; Burgos et al. 2018; Carreira-Rosario et al. 2018; Kohsaka et al. 2019). To increase coverage, we screened for Gal4 lines with sparse expression patterns, performed MultiColorFlpOut (Nern et al. 2015) to match their morphology to individual PMNs, and mapped neurotransmitter expression. We found 46 GABAergic (presumptive inhibitory), 22 glutamatergic (presumptive inhibitory), 100 cholinergic (presumptive excitatory), and 6 corozonergic (neuromodulatory) neurons; 62 PMNs could not be characterized due to lack of Gal4 lines (Figure 6K, Supplemental Table 1), and we did not identify any neurons co-expressing two fast neurotransmitters. A file that can be opened in CATMAID showing all 118 bilateral PMNs is provided as Supplemental File 2. Thus, we have identified a large majority of the PMN inputs to the MN population in segment A1.

Next we asked whether there are PMNs dedicated to innervating individual spatial or co-active muscle groups. We identified PMN pools that primarily target MNs innervating single spatial muscle groups, although many PMNs target multiple spatial muscle groups (Figure 7A). Similarly, we identified PMN pools that primarily target MNs innervating single forward co-active muscle groups, although many PMNs target multiple co-active muscle groups (Figure 7B). For example, PMNs in orange text preferred MNs innervating co-activated muscle group F2, whereas PMNs in green and dark blue text were targeted MNs in co-activated muscle group F3 and F4

respectively. More specifically, the A27h PMN (arrow in Figure 7B) has strong connections to the F3 MNs, and sparser connections to other co-activated groups. We used functional optogenetics to show that A27h activity onset followed the onset of F1/F2 pool of MNs (Figure 7C), consistent with preferential connectivity of A27h to F3 MNs (Figure 7B). Not surprisingly, we also identified PMN pools that primarily target MNs innervating single backward co-active muscle groups, although many PMNs target multiple co-active muscle groups (Figure 7D). We conclude that there are PMNs preferentially targeting individual co-activated muscle groups (consistent with a "labeled line" model), although there are many PMNs that innervate multiple co-activated muscle groups (consistent with a "combinatorial code" model).

Neuronal asymmetry linked to different muscle recruitment times during forward and backward locomotion

Neurons that are asymmetric along the anteroposterior axis are excellent candidates for differential recruitment during forward and backward locomotion. We found two MNs that are highly asymmetric: MN18 and MN25 (Figure 8A,B). In both cases, the asymmetric distribution of pre- and post-synaptic sites should lead to earlier activation during forward locomotion (for MN18) or during backward locomotion (for MN25). This is confirmed by the differential recruitment of their target muscles. Similar anterior/posterior asymmetry was observed in multiple PMNs: A02i and A03a4 have axons extending 1-2 segments anterior of the cell body and dendrites, and A01j and A03a5 have axons projecting 1-2 segments posterior to the cell body and dendrites (Figure 8C-F; Figure 3 – supplement 1). Due to the opposite direction of wave propagation in backward and forward locomotion, these PMNs are likely to contribute to the differential MN/muscle recruitment in forward and backward locomotion.

A recurrent network model that generates the observed forward and backward pattern of muscle activity

Recurrent interactions among PMNs have been shown to control the timing of the muscle outputs of central pattern generator circuits in a variety of organisms (Marder and Bucher 2001; Grillner 2003). We hypothesized that these types of interactions are responsible for the timing of muscle activation during *Drosophila* larval forward and backward crawling. To assess whether the reconstructed PMN connectome is capable of producing the observed timing of MN/muscle activation, we developed a recurrent network model of two adjacent segments. Previous models have focused on wave propagation during forward and backward crawling by modeling the average activity of excitatory and inhibitory subpopulations in each segment (Gjorgjieva et al. 2013; Pehlevan et al. 2016). Access to the detailed connectivity of PMNs and MNs (Supplemental Table 2 and Supplemental Table 3), as well as knowledge of the activation patterns of different co-activated muscle groups, allowed us to develop a substantially more detailed model whose circuitry was constrained to match the TEM reconstruction. For PMNs whose neurotransmitter identity we could determine, we also constrained the signs (excitatory or inhibitory) of connection strengths in the model. The firing rates of PMNs and MNs were modeled as simple threshold-linear functions of their synaptic inputs, and model parameters were adjusted to produce target MN patterns of activity that matched the sequences identified during forward and backward crawling. These patterns were assumed to be evoked by external command signals, representing descending input to the PMNs, that differed for forward and backward crawling but did not themselves contain information about the timing of individual muscle groups. We also constrained the activity of two PMNs, A18b and A27h, that are known to be specifically active during backward and forward locomotion, respectively (Fushiki et al. 2016; Carreira-Rosario et al. 2018). We found that, although the connectivity among PMNs within a segment is sparse (roughly 7% of all possible pairwise connections), the observed connections are nonetheless sufficient to generate appropriately timed MN activity for the two distinct behaviors (Figure 9A,B; Figure 9 – Figure supplement 1; see Methods). As has been described previously in other pattern-generating systems (Prinz et al. 2004), there is a space of models that is capable of

producing the observed activity. We therefore analyzed the activity of neurons in an ensemble of models. In the models, distinct sequences of PMN activity for forward and backward locomotion tile the period of time over which MNs are active (Figure 9C; Figure 9 – Figure supplement 1). These sequences give rise to the distinct timing of MN activation during each behavior. With the exception of *C. elegans* models (Karbowski et al. 2008; Macosko et al. 2009; Wen et al. 2012a; Izquierdo and Beer 2013; Izquierdo et al. 2015; Kunert et al. 2017; Rakowski and Karbowski 2017), the networks constructed here represent the first models of the neural circuitry underlying a timed motor behavior whose connectivity has been constrained by a synaptic wiring diagram.

Next we asked if the sequences of PMN activity predicted by the model are consistent with prior experimentally determined activity patterns. In our model, the PMN A14a is active at F1 and is inactive at F4 (Figure 9C). Similarly, experimental data show that A14a is inhibitory and is active during co-activated muscle group F1; and blocking A14a activity removes the contraction delay between muscles in co-activated muscle group F1 and F4 (Zwart et al. 2016), thereby validating our model. In our model, the PMNs A18b3 and A18a are both active during forward locomotion, but only A18a is active during backward locomotion (Figure 9C). Experimental data show that A18a and A18b3 are active precisely as proposed in our model (Hasegawa et al. 2016). Furthermore, our model predicts the cholinergic A18j and A01c PMNs are active at F4, which is supported by experimental data on these neurons (where they were called eIN1,2; Zwart et al. 2016).

To provide new, additional experimental tests of our model, we performed dual color calcium imaging on previously uncharacterized GABAergic PMNs A31k and A06l. Our model predicted that both A31k and A06l neurons show peak activity later than the early-activated MNs during both forward and backward locomotion (Figure 9C; Figure 9 – Figure supplement 1). To determine experimentally the phase-relationship between A31k and MNs, we expressed GCaMP6m in a subset of MNs and jRCaMP1b in A31k. Dual color calcium imaging data revealed that the A31k activity peak coincides with a decline of activity in MNs innervating early co-activated muscle groups during both forward and backward locomotion (Figure 10A,B), further validating our model. Second, our model predicts that both A31k and A06l PMNs show concurrent, rhythmic activity during forward and backward locomotion (Figure 9 – Figure supplement 1). We expressed GCaMP6m in both neurons, which we could distinguish based on their different axon projections, and found that they showed concurrent, rhythmic activity (Figure 10C,D), and thus both neurons show a delayed activation relative to MNs. Our third experimental test focused on the GABAergic A23a PMN (Schneider-Mizell et al. 2016). Our model predicted that A23a was active earlier during backward locomotion than forward locomotion (Figure 9C). We expressed GCaMP6m in a subset of MNs and jRCaMP1b in A23a, and validated the prediction of our model (Figure 10E,F). We conclude that our model accurately predicts many, but not all (see Discussion), of the experimentally determined PMN-MN phase relationships.

Circuit motifs specific for forward or backward locomotion

PMNs, in addition to connecting to MNs, make pre-synapses onto other neurons (Supplemental Table 3), generating circuit motifs that may play important roles during larval locomotion (Fushiki et al. 2016; Kohsaka et al. 2019). Interestingly, some of these PMNs are active only during forward or backward locomotion (Fushiki et al. 2016; Carreira-Rosario et al. 2018; Kohsaka et al. 2019), indicating they may change the dynamics of motor circuits during forward versus backward locomotion, resulting in different muscle activity patterns during forward or backward crawling. Here we used connectome and neurotransmitter data to examine circuit motifs that include these direction-specific PMNs and asked how they can contribute to the generation of different coactive muscle groups during forward and backward locomotion.

The previously described forward-specific excitatory PMN A27h (Fushiki et al. 2016; Carreira-Rosario et al. 2018), with F3 onset, connects to the excitatory PMNs A18b2 and A18b3 innervating F1-F4 MNs. Thus, when A27h activates F3, it also maintains activity of A18b2 and A18b3 to ensure continued excitation of F1/F2

MNs (Figure 11A). These motifs provide testable hypotheses for how specific phase relationships between co-activated muscle groups are generated by PMNs. Furthermore, A27h is a component of feedforward excitatory and inhibitory motifs that could explain how different co-activated muscle groups in the adjacent segments are coordinated. A27h innervates the excitatory PMN A18b3 in the next anterior segment, which could advance the forward contraction wave, while A18b3 excites the inhibitory PMNs A06c/A14a to prevent premature activation of F3/4 MNs in the next adjacent segment (Figure 11B). Another forward-specific PMN A01d3 (also known as ifb-FWD) (Kohsaka et al. 2019), is also a component of feedforward excitation and feedforward inhibition motifs involved in temporally segregating F1-F3 from F4 coactive-muscle groups (Figure 11C).

Next, we examined circuit motifs composed of a backward-specific PMN, A27k (also known as ifb-BWD) locomotion (Kohsaka et al. 2019). We identified both feedforward excitation and feedforward inhibition motifs that could explain the sequential activation of a specific co-activated muscle group in adjacent segments during backward motor waves. A27k (innervating B4) is involved in a feedforward inhibitory circuit in which it excites the inhibitory local PMNs A02e and A02g (innervating B1/B2). This motif could coordinate excitation of B3/B4 MNs and termination of B1/B2 MN activity as the contraction wave moves posteriorly (Figure 11D). A27k also synapses in the next anterior segment with the excitatory neurons A01c1, A01c2, and A18j (innervating B4), as well as with the inhibitory PMN A02e innervating B1/B2. This could coordinately terminate B1/B2 MN activity and activate B4 MN activity (Figure 11E). We conclude that circuit motifs composed of forward or backward specific PMNs are likely to be an additional mechanism for generating distinct forward or backward coactivated muscle groups. Functional examination of these motifs is beyond the scope of the current study.

Discussion

It is a major goal of neuroscience to comprehensively reconstruct neuronal circuits that generate specific behaviors, but to date this has been done only in *C. elegans* (Karbowski et al. 2008; Macosko et al. 2009; Izquierdo and Beer 2013; Izquierdo et al. 2015; Kunert et al. 2017; Rakowski and Karbowski 2017). Recent studies in mice and zebrafish have shed light on the overall distribution of PMNs and their connections to several well-defined MN pools (Eklof-Ljunggren et al. 2012; Kimura et al. 2013; Bagnall and McLean 2014; Ljunggren et al. 2014). However, in mouse and zebrafish it remains unknown if there are additional PMNs that have yet to be characterized, and the connectivity between PMNs is not well described, which would be important for understanding the network properties that produce coordinated motor output. In the locomotor central pattern generator circuitry of leech, lamprey, and crayfish, the synaptic connectivity between PMNs or between PMNs and other interneurons are known to play critical roles in regulating the swimming behavior (Brodfuehrer and Thorogood 2001; Grillner 2003; Kristan et al. 2005; Mullins et al. 2011; Mulloney and Smarandache-Wellmann 2012; Mulloney et al. 2014). However, it is difficult to be certain that all the neural components and connections of these circuits have been identified. The comprehensive anatomical circuitry reconstructed in our study provides an anatomical constraint on the functional connectivity used to drive larval locomotion; all synaptically-connected neurons may not be relevant, but at least no highly connected local PMNs are absent from our analysis.

Our results confirm and extend previous studies of *Drosophila* larval locomotion. For example, a recent study (Zwart et al. 2016) has shown that the GABAergic A14a inhibitory PMN (also called iIN1) selectively inhibits MNs innervating muscle 22/LT2 (co-activated muscle group F4), thereby delaying muscle contraction relative to muscle 5/LO1 (co-activated muscle group F2). We extend this study by showing that A14a also disinhibits MNs in early co-activated muscle groups F1/2 via the inhibitory PMN A02e. Thus, A14a both inhibits late co-activated muscle groups and disinhibits early co-activated muscle groups. In addition, previous work has suggested that all MNs receive simultaneous excitatory inputs from different cholinergic PMNs (Zwart et al. 2016). However, our dual calcium imaging data of the A27h excitatory PMN shows that it is active during co-

activated muscle group F3 and not earlier. Therefore, MNs may receive temporally distinct excitatory inputs, in addition to the previously reported temporally distinct inhibitory inputs. We have identified dozens of new PMNs that are candidates for regulating motor rhythms; functional analysis of all of these PMNs is beyond the scope of this paper, particularly due to the additional work required to screen and identify Gal4/LexA lines selectively targeting these PMNs, but our predictions are clear and testable when reagents become available.

We show that MNs innervating a single spatial muscle group can belong to more than one co-activated muscle group, therefore spatial muscle groups do not invariably match co-activated muscle groups. This could be due to several reasons: (i) MNs in each spatial muscle groups receive inputs from overlapping but not identical array of PMNs (Supplementary Table 1). (ii) Different MNs in the same spatial muscle group receive a different number of synapses from the same PMN (Supplementary Table 1). (iii) MNs in the same spatial muscle group vary in overall dendritic size and total number of post-synapses (Supplementary Table 1), thereby resulting in MNs of the same spatial muscle group falling into different co-activated muscle groups.

We demonstrate that during both forward and backward locomotion, most of longitudinal and transverse muscles of a given segment contract as early and late groups, respectively. In contrast, muscles with oblique or acute orientation often show different phase relationships during forward and backward crawling. Future studies will be needed to provide a biomechanical explanation for why oblique muscles – but not longitudinal or transverse muscles – need to be recruited differentially during forward or backward crawling. Also, it will be interesting to determine whether the VO or VL MNs are responsible for elevating cuticular denticles during propagation of the peristaltic wave; if the VOs, it would mean that lifting the denticles occurs at different phases of the crawl cycle in forward and backward locomotion.

Our recurrent network model accurately predicts the order of activation of specific PMNs, yet many of its parameters remain unconstrained, and some PMNs may have biological activity inconsistent with activity predicted by our model. Sources of uncertainty in the model include incomplete reconstruction of inter-segmental connectivity and descending command inputs, the potential role of gap junctions (which are not resolved in the TEM reconstruction), as well as incomplete characterization of PMN and MN biophysical properties. Recent studies have suggested that models constrained by TEM reconstructions of neuronal connectivity are capable of predicting features of neuronal activity and function in the *Drosophila* olfactory (Eichler et al. 2017) and visual (Takemura et al. 2013; Tschopp et al. 2018) systems, despite the unavoidable uncertainty in some model parameters and the likely presence of multiple distinct models that produce activity consistent with recordings (Prinz et al. 2004; Brenner 2010; Bargmann and Marder 2013). For the locomotor circuit described here, we anticipate that the addition of model constraints from future experiments will lead to progressively more accurate models of PMN and MN dynamics. Despite its limitations, the ability of the PMN network to generate appropriate muscle timing for two distinct behaviors in the absence of third-layer or command-like interneurons suggests that a single layer of recurrent circuitry is sufficient to generate multiple behavioral outputs. It is also notable that a model lacking complex single-neuron dynamics such as post-inhibitory rebound or spike-frequency adaptation, which are critical for modeling other central pattern generator circuits (Marder and Bucher 2001), is sufficient to produce the observed motor pattern. Thus, although there are likely complex intrinsic neuronal dynamics that our model fails to capture, recurrent excitatory and inhibitory interactions may play a large role in establishing appropriate motor timing in the larva.

Previous work in other animal models have identified multifunctional muscles involved in more than one motor behavior: swimming and crawling in *C. elegans* (Pierce-Shimomura et al. 2008; Vidal-Gadea et al. 2011; Butler et al. 2015) and leech (Briggman and Kristan 2006); walking and flight in locust (Ramirez and Pearson 1988); respiratory and non-respiratory functions of mammalian diaphragm muscle (Lieske et al. 2000; Fogarty et al. 2018) unifunctional muscles which are only active in one specific behavior in the lobster *Homarus americanus* (Mulloney et al. 2014); swimming in the marine mollusk *Tritonia diomedea* (Popescu and Frost 2002); and muscles

in different regions of crab and lobster stomach (Bucher et al. 2006; Briggman and Kristan 2008). Our single-muscle calcium imaging data indicates that all imaged larval body wall muscles are bifunctional and are activated during both forward and backward locomotion. It will be interesting to determine if all imaged muscles are also involved in other larval behaviors, such as escape rolling, self-righting, turning, or digging. It is likely that there are different co-activated muscle groups for each behavior, as we have seen for forward and backward locomotion, raising the question of how different co-activated muscle groups are generated for each distinct behavior.

Methods

Electron microscopy and CATMAID reconstructions

Neurons were reconstructed in CATMAID using a Google Chrome browser as previously described (Ohyama et al. 2015). Candidate PMNs were discarded if their maximum MN connectivity was ≤5 synapses (summed across the left and right hemispheres), where the neuron could not be traced due to gaps in the TEM volume, and a few neurons with massive arbors which were beyond our ability to trace. Figures were generated using CATMAID graph or 3D widgets combined with Adobe Illustrator (Adobe, San Jose, CA).

Synapse spatial distributions and clustering

Synapse spatial distributions were generated using custom MATLAB scripts. Spatial distributions were determined using kernel density estimates with a 1 μm bandwidth. For cross-sectional spatial distributions, points were rotated -12 degrees around the Z-axis (A/P axis) in order to account for the slight offset of the EM-volume. For pre-synaptic sites, polyadic synapses were weighted by their number of post-synaptic targets. Synapse similarity was calculated as described previously (Schlegel et al. 2016):

$$f(is,jk) = e^{\frac{-d_{sk}^2}{2\sigma^2}} e^{\frac{|n_{is}-n_{jk}|}{n_{is}+n_{jk}}}$$

where *f(is,jk)* is the mean synapse similarity between all synapses of neuron *i* and neuron *j*. d_{sk} is the Euclidean distance between synapses *s* and *k* such that synapse *k* is the closest synapse of neuron *j* to synapse s of neuron *i*. σ is a bandwidth term that determines what is considered close. n_{is} and n_{jk} are the fraction of synapses for neuron *i* and neuron *j* that are within ω of synapse *s* and synapse *k* respectively. For MN inputs, σ = ω = 2 μm. Clustering was performed by using the average synapse similarity scores for the left and right hemisegments as a distance metric, and linkage was calculated using the average synapse similarity. For comparing the distributions across individual axes, a two sample Kolmogorov-Smirnov test was used to determine significance.

Clustering analysis of PMN-MN connectivity

Weighted PMNs to MNs connectivity matrix was acquired from CATMAID TEM volume as percentage of total number of post-synaptic links to these target MNs. We then calculated the average of left and right pairs of PMNs and MNs. Next, we averaged the mean connections from PMNs to all MNs innervating muscle groups defined in Figure 7A, B, and D. Hierarchical clustering was performed on these averaged connectivity matrixes using Python's seaborn.clustermap (standard_scale=0, metric= correlation, method= single, https://seaborn.pydata.org/generated/seaborn.clustermap.html).

Muscle GCaMP6f imaging, length measurement, and quantification

2% melted agarose was used to make pads with similar size: 25mm (W) X 50mm (L) X 2mm (H). Using tungsten wire, a shallow ditch was made on agarose pads to accommodate the larva. To do muscle ratiometric calcium imaging in intact animals, a first or second instar larvae expressing GCaMP6f and mCherry in body wall

muscles were washed with distilled water, then moved into a 2% agarose pad on the slide. A 22 mm × 40 mm cover glass was put on the larva and pressed gently to gently constrain larval locomotion. The larva was mounted dorsolaterally or ventrolaterally to image a different set of muscles (dorsolateral mount excludes the most ventral muscles (15,16,17) whereas the ventrolateral mount excludes the dorsal-most muscles (1,2,9,10); imaging was done with a 10x objective on an upright Zeiss LSM800 microscope. We recorded a total of 38 waves (24 forward and 14 backward) from four different animals, and examined muscle calcium activity in two subsequent hemi-segments for each wave. Muscle length measurement was done using custom MATLAB scripts where muscle length was measured on a frame by frame basis. Calcium imaging data was also analyzed using custom MATLAB scripts. Due to movement artifacts, ROIs were updated on a frame by frame basis to track the muscle movement. ROIs that crossed other muscles during contraction were discarded. In no single preparation was it possible to obtain calcium traces for all 30 muscles. Instead, we used only preparations in which at least 40% of the muscles could be recorded. In order to align crawl cycles that were of variable time and muscle composition, we first produced a 2 dimensional representation of each crawl cycle using PCA. Crawl cycles were represented as circular trajectories away from, and back towards the origin (Figure 3 – figure supplement 1E,F) similar to what has been shown previously (Lemon et al. 2015). The amplitude, or linear distance from the origin, to a point on this trajectory correlated well with both the coherence of the calcium signals as well as the amplitude of the population. Thus, peaks in this 2D amplitude correspond with the time in which most muscles are maximally active, which we defined as the midpoint of a crawl cycle. It should be noted that the muscles used to generate two dimensional representations of crawl cycles were different for each crawl. While this means that each PCA trajectory is slightly different for each crawl cycle, we reasoned that because each experiment contained muscles from every co-activated muscle group, the peak amplitude in PCA space should still correspond to a good approximation of the midpoint of the crawl cycle. We defined the width of a crawl cycle as the width of this 2D peak at half-height (Figure 3 – figure supplement 1G). We aligned all crawl cycles to the crawl onset and offset (which we call 25% and 75% of the crawl cycle respectively) as defined by this width at half-height (Figure 3 – figure supplement 1H,I).

Calcium imaging in neurons

For dual-color and single-color calcium imaging in fictive preps, freshly dissected brains were mounted on 12mm round Poly-D-Lysine Coverslips (Corning® BioCoat™) in HL3.1 saline (de Castro et al. 2014), which were then were placed on 25 mm × 75 mm glass slides to be imaged with a 40× objective on an upright Zeiss LSM-800 confocal microscopy. To simultaneously image two different neurons expressing GCaMP6m we imaged neuron-specific regions of interest (ROI). In addition, we imaged two neurons differentially expressing GCaMP6m and jRCaMP1b. Image data were imported into Fiji (https://imagej.net/fiji) and GCaMP6m and jRCaMP1b channels were separated. The $\Delta F/F_0$ of each ROI was calculated as $(F-F_0)/F_0$, where F_0 was averaged over ~1s immediately before the start of the forward or backward waves in each ROI.

Antibody staining and imaging

Standard confocal microscopy, immunocytochemistry and MCFO methods were performed as previously described for larvae (Carreira-Rosario et al. 2018). Primary antibodies used: GFP or Venus (rabbit, 1:500, ThermoFisher, Waltham, MA; chicken 1:1000, Abcam13970, Eugene, OR), GFP or Citrine (Camelid sdAB direct labeled with AbberiorStar635P, 1:1000, NanoTab Biotech., Gottingen, Germany), GABA (rabbit, 1:1000, Sigma, St. Louis, MO), mCherry (rabbit, 1:1000, Novus, Littleton, CO), HA (mouse, 1:200, Cell Signaling, Danvers, MA), or V5 (rabbit, 1:400, Rockland, Atlanta, GA), Flag (rabbit, 1:200, Rockland, Atlanta, GA). Secondary antibodies were from Jackson Immunoresearch (West Grove, PA) and used according to manufacturer's instructions. Confocal image stacks were acquired on Zeiss 710 or 800 microscopes. Images

were processed in Fiji (https://imagej.net/Fiji), Photoshop, and Illustrator (Adobe, San Jose, CA). Brightness and contrast adjustments were applied to the entire image uniformly; mosaic images were assembled in Photoshop (Adobe, San Jose, CA).

Recurrent network model

Model dynamics

We constructed a recurrent network representing the activity of PMNs, which we denote by the vector $\mathbf{p}$, and of MNs, which we denote by the vector $\mathbf{m}$. The firing rate of PMN or MN i is a rectified-linear function of its input: $p_i(t) = [u_i^p(t)]_+$ or $m_i(t) = [u_i^m(t)]_+$, where $[\cdot]_+$ denotes rectification. The PMN input $\mathbf{u}^p$ follows the differential equation:

$$\boldsymbol{\tau}^p \odot \frac{d\mathbf{u}^p}{dt} = -\mathbf{u}^p(t) + \mathbf{g}^p \odot (\mathbf{J}^p\mathbf{p}(t) + \mathbf{b}^p + \mathbf{I}(t)),$$

where τ_i^p is the time constant of PMN i, b_i^p its baseline excitability, $I_i(t)$ its descending input from other regions, $\odot$ denotes element-wise multiplication, and $\mathbf{J}^p$ is the connectivity matrix among PMNs. We also include a neuron-specific gain term g_i^p which determines how sensitive a PMN is to its inputs (this is required because we fix the scale of $\mathbf{J}$ based on the TEM reconstruction). The descending input to the PMNs $\mathbf{I}(t)$ is represented as a pulse of activity: $\mathbf{I}(t) = \mathbf{I}^{FWD}$ during FWD crawling, $\mathbf{I}(t) = \mathbf{I}^{BWD}$ during BWD crawling, and $\mathbf{I}(t) = 0$ otherwise.

MNs follow similar dynamics:

$$\boldsymbol{\tau}^m \odot \frac{d\mathbf{u}^m}{dt} = -\mathbf{u}^m(t) + \mathbf{g}^m \odot (\mathbf{J}^m\mathbf{p}(t) + \mathbf{b}^m),$$

where $\mathbf{J}^m$ is the connectivity matrix from PMNs to MNs.

To generate PMNs and MNs corresponding to the A2 segment, we duplicated the A1 MNs and the PMNs we reconstructed for which no corresponding neuron in the next anterior segment was reconstructed. This produces a connectivity matrix with an approximate block structure:

$$\mathbf{J}^p = \begin{pmatrix} \mathbf{J}_{11}^p & \mathbf{J}_{12}^p \\ \mathbf{J}_{21}^p & \mathbf{J}_{22}^p \end{pmatrix},\ \mathbf{J}^m = \begin{pmatrix} \mathbf{J}_{11}^m & \mathbf{J}_{12}^m \\ \mathbf{J}_{21}^m & \mathbf{J}_{22}^m \end{pmatrix},$$

where $\mathbf{J}_{rs}^{p/m}$ represents connections from segment r to segment s.

Target activity

The model parameters ($\mathbf{J}$, $\mathbf{g}$, $\mathbf{b}$, $\boldsymbol{\tau}$, $\mathbf{I}$) are adjusted using gradient descent so that the MN activity $\mathbf{m}$ reproduces target patterns of activity during FWD and BWD crawling. These targets are defined for 6 s trials that contain one sequence of CMUG activation in each of the two segments. Time is discretized into 50 ms bins. At the beginning of each trial, $\mathbf{u}^p$ is initialized with random values from a truncated Gaussian distribution with standard deviation 0.1, and $\mathbf{u}^m$ is initialized to 0. A trial consists of sequential activity in each segment with a 1 s inter-segmental delay (Figure 9). Trials begin and end with 1 and 1.5 s of quiescence, respectively. Each MN's target activity is given by a rectified cosine pulse of activity whose start and end times depend on the CMUG to which it belongs.

The first CMUG is active for 2 s, and subsequent CMUGs activate with a delay of 0.25 s between each group and end with a delay of 0.125 s between groups. The participation of MNs in CMUGs and the order in which the segments are active during FWD and BWD crawling are inferred from the data (Figure 3).

Parameter constraints and optimization

Constraints are placed on the model parameters based on knowledge of the circuit. The nonzero elements of $\mathbf{J}^p$ and $\mathbf{J}^m$ are determined from the TEM reconstruction (normalized based on the percent input received by the post-synaptic target), and signs are constrained using neurotransmitter identity when available. If the neurotransmitter identity of a neuron is not known, we initialize the connection to be inhibitory but do not constrain its sign during optimization. Time constants $\boldsymbol{\tau}$ are constrained to be between 50 ms and 1 s (these represent combined membrane and synaptic time constants), and gains $\mathbf{g}$ are constrained to be positive.

At the beginning of optimization, the biases $\mathbf{b}^p$ and $\mathbf{b}^m$ are initialized equal to 0.1 and 0, respectively. Time constants $\boldsymbol{\tau}$ are initialized to 200 ms and gains $\mathbf{g}$ to 1. $\mathbf{I}^{FWD}$ and $\mathbf{I}^{BWD}$ are initialized uniformly between 0.05 and 0.15 for each neuron. To initialize $\mathbf{J}^p$ and $\mathbf{J}^m$, initial connection strengths are taken in proportion to synapse counts from the TEM reconstruction with a scaling factor of ± 0.005 for excitatory/inhibitory connections. Connections within a model segment are taken from the TEM reconstruction of A1, while connections from A1 to A2 or A2 to A1 are taken from the corresponding cross-segmental reconstructions (and are thus likely less complete than the within-segmental connectivity).

The cost function that is optimized consists of a term C_{targ} that penalizes deviations of the MN activities from their targets and three regularization terms to promote realistic solutions. The target term is given by $C_{targ} = \sum_{t,i} w_i \, ||m_i(t) - m_i^*(t)||^2$, where $m_i^*(t)$ is the target activity for MN i and w_i is a weighting term, proportional to $1/\sqrt{N_{CMUG,i}}$ where $N_{CMUG,i}$ is the number of neurons in the CMUG of neuron i (this scaling ensures the target patterns of CMUGs with few MNs are still reproduced accurately).

The first regularization term is given by $C_{A18b,A27h} = 0.05 \cdot (\sum_{t \in FWD} |p_{A18}(t)| + \sum_{t \in BWD} |p_{A27}(t)|)$, which suppresses the activity of the A18b and A27h neurons for behaviors during which they are known to be quiescent. The second regularization term C_{seg} constrains PMN activity to reflect the timing of segmental activation. It is given by

$$C_{seg} = \alpha_n \sum_{t \in active1} ||\mathbf{p}_1(t) - \mathbf{p}_2(t - t_{delay})||^2 ,$$

where active1 represents the times when segment 1 is active, $\mathbf{p}_1$ and $\mathbf{p}_2$ represent vectors of PMN activities corresponding to pairs of homologous neurons in adjacent segments, and t_{delay} is the time delay between segment 1 and 2 activations (equal to -1 s for forward and +1 s for backward crawling). This term ensures that PMN activity in the A1 and the A2 segments is similar but offset in time. The scaling term α_n increases quadratically from 0 to 0.1 over the 1000 training epochs. The final term $C_J = \alpha_n\left(||\mathbf{J}^p - \mathbf{J}_0^p||^2 + ||\mathbf{J}^m - \mathbf{J}_0^m||^2\right)$ penalizes deviations of model weights from the initial weights given by the TEM reconstruction.

The total cost, equal to $C_{targ} + C_{A18b,A27h} + C_{seg} + C_J$, is optimized using the RMSProp optimizer for 1000 epochs. During each epoch, the costs corresponding to one FWD and one BWD trial are averaged. The learning rate decreases from 10^{-2} to 10^{-3} logarithmically over the course of optimization.

Acknowledgements

We thank Luis Sullivan, Emily Sales, and Hiroshi Kohsaka for comments. B.M. was supported by an NIH training grant T32HD007348. A.C. was supported by HHMI. A.L.-K. was supported by the Burroughs Wellcome Foundation, the Gatsby Charitable Foundation, the Simons Collaboration on the Global Brain, and NSF award DBI-1707398. C.Q.D. and A.A.Z were supported by HHMI and NIH HD27056.

609 **Table 1. Motor neurons present in the CATMAID reconstruction.**
610 All MNs were identified in the first abdominal segment on both left and right sides, with the exception of MN25
611 which is not present in A1 and thus annotated in A2. See text for abbreviations.
612

Spatial Muscle Group	Nerve	Motor neurons (synonyms)	Target Muscles (synonyms)	Synapse Type
DL	ISN^{DM}	MN1 (aCC)	1 (DA1)	Ib
	ISN^{DM}	MN2 (U3)	2 (DA2)	Ib
	ISN^{DM}	MN3 (U4)	3 (DA3)	Ib
	ISN^{DM}	MN4 (U5)	4 (LL1)	Ib
	ISN^{DM}	MN9 (U1)	9 (DO1)	Ib
	ISN^{DM}	MN10 (U2)	10 (DO2)	Ib
DO	ISN^{L}	MN11	11 (DO3)	Ib
	ISN^{L}	MN19	19 (DO4)	Ib
	ISN^{L}	MN20	20 (DO5)	Ib
	SNa	MN5 (LO1)	5 (LO1)	Ib
VL	ISNb	MN6/7 (RP3)	6/7 (VL3/VL4)	Ib
	ISNb	MN12 (V-MN)	12 (VL1)	III
	ISNb	MN13 (MN-VL2)	13 (VL2)	Ib
	ISNb	MN14 (RP1)	14 (VO2)	Ib
	ISNb	MN30 (RP4)	30 (VO1)	Ib
VA	SNc	MN26	26 (VA1)	Ib
	SNc	MN27	27 (VA2)	Ib
	SNc	MN29	29 (VA3)	Ib
VO	ISNd	MN15/16 (MN-VO4/5)	15/16 (VO4/VO5)	Ib
	ISNd	MN15/16/17 (MN-VO4-6)	15/16/17 (VO4/VO5/VO6)	Ib
	ISNb	MN28	28 (VO3)	Ib
T	SNa	MN8 (SBM)	8 (SBM)	Ib
	SNa	MN21/22 (LT1/LT2)	21/22 (LT1/LT2)	Ib
	SNa	MN22/23 (LT2/LT3)	22/23 (LT2/LT3)	Ib
	SNa	MN23/24 (LT3/LT4)	23/24 (LT3/LT4)	Ib
	ISN^{L}	MN18	18 (DT1)	Ib
	TN	MN25 (VT1)	25 (VT1)	Ib
Broad	ISN^{DM}	MNISN (RP2)	1/2/3/4/9/10/11/[18]/19/20 (DA/DO)	Is
	ISNb	MNISNb/d (RP5)	6/7/12/13/14/15/16/30 (VL/VO)	Is
	SNa	MNSNa-II (VUM)	21/22/[23/24/25] (LT)	II
	ISN^{DM}	MNISN-II (VUM)	1/2/3/4/9/10/11/18/19/20 (DA/DO)	II
	ISNb	MNISNb/d-II (VUM)	12/13/14/15/16/17/30 (VL/VO)	II

613
614

Table 2. Co-activated muscle groups during forward or backward locomotion.
There are four co-activated muscle groups during backward and forward locomotion, but the muscles in each group differ in forward versus backward locomotion. Note that backward locomotion is not simple a reverse of the pattern seen in forward locomotion. This represents the most common activation sequences, although there is some variation, particularly during the fastest locomotor velocities.

Forward	Co-activated muscles
F1	2,6,10,11,14,30
F2	3,4,5,9,12,13,18,19,25,26,29
F3	1,8,15,16,17,20,28
F4	21,22,23

Backward	Co-activated muscles
B1	10,15,16,17
B2	1,3,4,6,9,12,13,28
B3	2,5,8,19,20,26,29
B4	11,18,21,22,23,24

Table 3. Premotor neurons innervating type Ib MNs

Left column, spatial muscle groups named as in Figure 1. Middle column, type Ib MNs innervating 1-3 muscles in each muscle group (synonym, parentheses); the immature neuromodulatory VUMs are not shown. Right column, premotor interneurons innervating the indicated MNs (green, presumed excitatory; red, presumed inhibitory; grey, corozonergic; black, unknown. Premotor connectivity uncertain, parentheses.

Muscle position	Motor Neurons	Pre-Motor Neurons
DL	MN1-Ib (aCC)	A27h, A18a, A18b, A03g, A31k, A31b, A06e, A23a, A02h, A10e, A03a1, A03a3, A05k, A07f2, DLN2, TJPMN, Thoracic descending pre-longitudinals, T27Y, dsnPMN2, DLN1, A18neo
	MN2-Ib (U3)	A01x2, A18a, A03a5, A31k, A31b, A23a, A02h, A03a3, A03a1, A10e, A10a , T27Y, dsnPMN2,
	MN3-Ib (U4)	A18a, A03a5 A03g, A31k, A31b, A06e, A02h, A02e, A02f, A03a3, A03a6, A03d/e, A03x-eghb, A07f2, A10a, DLN2, A18neo
	MN4-Ib (U5)	A03a5, A03g, A31k, A27l, A06l, A06m, A06g2, A02e, A02f, A03a6, A03a1, A03x-eghb, SePN02b, DLN2, Descending pre RP3, A18neo
	MN9-Ib (U1)	A01x2, A18a, A31k, A31b, A06x1, A27l, A23a, A02m, A02n, A02h, A03a1, A03a3, A03x-eghb, A03xyz, A05k, DLN2, TJPMN, Tipsi, T27Y, dsnPMN2, DLN1, A18neo,
	MN10-Ib (U2)	A01x2, A18b, A08e1, A31k, A27j, A23a, A06a, A06x1, A02h, A02e, A02g, A10e, A03a1, A03a3, A03x, A03a4, A03d/e, A03x-eghb, VLELX4, Tipsi, dsnPMN2, DLN2, DLN1, A18neo, A18c
DO	MN11-Ib	A31k, A06x1, A23a, A06a, A27l, T03g2, A03a1, A03a3, A03x-eghb
	MN19-Ib	A27k, A18j, A18b, A18b3, T01d2, A31k, A27j, A23a, A06a, A06l, A06x1, A02f, A03a1, A03a3, T27Y, dsnPMN2, A27neo
	MN20-Ib	A27h, A18j, A01c1, T01d2, T01d4, A19l, A06e, A03d/e, A27neo, a14neo, A03xyz, A26f
	MN5-Ib (LO1)	A18b3, A18b2, A23a, A03a1, A03a3, A03a4, VLELX4, T27Y
VL	MN6/7-Ib (RP3)	A18b3, A03a5, A27l, A06l, A06e, A02g, A02e, A03a4, T)6WW, T06PP, Descending pre RP3,
	MN12-III (V-MN)	A27h, A03a5, A03g, A02g, A02e A27l, A06l,, A06e A03a6, A03a4, A03d/e, DLN1, Descending pre RP3,
	MN13-Ib (MN-VL2)	A27k, A03a5, A03g, A01d3, T01d4, A06l, A06a, A06e, A02g, A02e, A27l, A03a6, A03a4, A03x-eghb, A03d/e
	MN14-Ib (RP1)	A27h, A18b2, A18b3, A27l, A06l, A02i, A03a4, A03a1, DLN1
	MN30-Ib (RP4)	A18b3, A03a5, A01x2, A01d3,A01d4, A06e , A27l, A06l, A02g, A02e, A03a4, A03a6, A03x-eghb, A03d/e, A03SNC, A10a, A27Uniq, DLN1, A03xyz, SePN02b
VA	MN26-Ib	A27h, A01x3, A18f, A02j, A06e, A06l, A27l, T03g2, A03x-eghb, Descending neuron_SEZ, A03SNC, A03xKT, , A03d/e, T11v, T27Y,
	MN27-Ib	A27h, A27k, A03g, A18j, A18f, A01x3, A01c1, A01c2, T01d2, T01d4, A06e, A06f, A19l, A14a, A31b, T03g2, A27n, , A27neo, A03xKT, T11v, A26f
	MN29-Ib	A01x3, A01x2, A01x3, T01d2, T01d4, A27l, A02g, A06e, T03g2, A27e2, A03a6, A03d/e, A10a, A27neo, T11v, A03SNC
VO	MN15/16-Ib	A27h, A27k, A18b2, A06c, A06l, A06e, A02g, A02i, A03a6, DLN1
	MN15/16/17-Ib	A27h, A03g, A06c, A06e, A27l, A02g, A02i, A01j, A27Uniq,
	MN28-Ib	A01x2, A27h, A18b2, A06c, A06l, A06e, A02g, A02i, A03a6
T	MN8-1b (SBM)	A01c1, A01c2, A01d3, A27k, A03g, T01d1, A18j, A19l, A14a, A27n, A27e2, A27neo, A26f
	MN18-Ib	A01c1, A01c2, A01d3, A03g, A03o, A18j, A06a, A23a, A19l, A14a, A06x1, A02i, A01j, A27n, A10a, A10b, A27neo, T27Y, A26f
	MN21/22-Ib (LT1/LT2)	A01c1, A01c2, A27k, A03g, A18j, A18b2, T01d1, T01d2, A19l, A14a, A02i,A02f, A03xKT, T27Y, TGun, A27n, A27neo, A26f
	MN22/23-1b (LT2/LT3)	A01x, A01c1, A01c2, A27k, A03g, A09l, A18j, T01d1, T01d2, A01d3, A19l, A14a, A02f, A27n, A27neo, A27e2, T27Y, A26f
	MN23/24-1b (LT3/LT4)	A27k, A18j, A03g, A01c1, A01c2, T01d1, T01d2, A01d3, A19l, A27n, A27neo, A26f
	MN25-Ib (MN-VT1)	A01c1, A18a, A18b2, A18j, A18f, A27l, A14a, A19l, A02i, A31d, A03xKT, A05a
DL/DO	MNISN (RP2)	A01x2, A18b, A03g, A31k, A27j, A27l, A02m, A02n, A02b, A06a, A23a, A03a1, A03a3, A03d/e, A03x-eghb, A05k, A10a, DLN2, DLN1, A18neo, dsnPMN2, SePN02b, T27Y, TJPMN, Projection neuron, A18c,
VL/VO	MSNISNb/d(RP5)	A27h, A03a5, A06l, A06c, A06f, A02g, A02e, A02b, A03a4, A03a6, A03x-eghb, A03d/e, A19d, A27Uniq, DLN1, SePN02b

Figure 1. Schematic depiction of the larval neuromuscular system.
(A) *Drosophila* larva contain three thoracic and nine abdominal segments, the muscles of which are innervated by MNs located in the corresponding thoracic and abdominal segments of the CNS.
(B) Schematic of the 30 muscles of abdominal segments (A2-A6) from internal and external view. Segment A1 is similar to A2-A6, with the exception that it lacks muscle 25 and MN-25.

Figure 2. All body wall muscles are utilized during forward and backward locomotion.
(A,D) Sequential images of muscle GCaMP6f ΔF/F signal during forward (A) or backward (D) locomotion. GCaMP6f levels were normalized to mCherry. Anterior to left, dorsal up; time in seconds. Genotype: *GMR44H10-LexA lexAOP-GCaMP6f; -LexA lexAOP--mCherry.* Arrowheads mark the same segment at each timepoint.
(B,E) Mean calcium transient (blue) vs mean muscle length (red) measurements for muscle 6 during forward (B) or backward (E) locomotion. N = 3 segments. T_0 was set as the point of maximum contraction as determined by muscle length for each crawl. Shaded bars represent standard deviation.
(C,F) All observed muscles show calcium transients greater than 100% ΔF/F during forward (C) or backward (F) locomotion. Each dot represents the maximum GCaMP ΔF/F signal in the indicated muscle during a single crawl, normalized to mCherry. Error bars represent standard deviation. Muscle names as in Figure 1.

Figure 3. Larval body wall muscles form four co-activated muscle groups during forward and backward locomotion
(A) Hierarchical clustering of mean activity for all observed muscles yields four co-activated muscle groups during forward locomotion (F1-F4) and a different group of four during backward locomotion (B1-B4). Heatmaps represent the mean range-normalized calcium activity of each muscle (n > 3 forward crawl bouts for each muscle, with a total of 337 individual muscles analyzed across 23 crawls for forward and 188 individual muscles analyzed across 14 crawls for backward locomotion). Muscles 6/7 are grouped because they are both innervated by the same MN. Clustering was performed only on the first half of the crawl cycle to determine the onset time for each co-activated muscle group. Cluster number was determined by visual inspection of the dendrogram as well as the gap-criterion optimal cluster number.
(B) Plots of average muscle activity for muscles in each forward co-activated muscle group. Error bars represent the standard deviation of individual muscles.
(C) Plots of average forward co-activated muscle group activity timing. Error bars represent the standard deviation of the average muscle activity of each muscle in a given co-activated muscle group. Dotted lines represent the average muscle activity for each muscle in a given co-activated muscle group. Red line along the x-axis represents the fraction of the crawl cycle that was used for clustering.
(D) Plots of average muscle activity for muscles in each backward co-activated muscle group. Error bars represent the standard deviation of individual muscles.
(E) Plots of average backward co-activated muscle group activity timing. Error bars represent the standard deviation of the average muscle activity of each muscle in a given co-activated muscle group. Dotted lines represent the average muscle activity for each muscle in a given co-activated muscle group. Red line along the x-axis represents the fraction of the crawl cycle that was used for clustering.
(F) Schematic representation of the co-activated muscle group for forward locomotion.
(G) Schematic representation of the co-activated muscle group for backward locomotion.
(H) During forward locomotion, muscle 11 is activated before muscle 15-17, while their order is flipped during backward crawling.

Figure 4. Identification of all differentiated motor neurons in segment A1 of the TEM volume.
(A) Dorsal view of the TEM reconstruction of the L1 CNS (gray shading) showing all bilateral MNs reconstructed at single synapse level. The one intersegmental dendrite is from RP3 in A1; it is not observed in other abdominal segments.
(B) Dorsal view of centered on the A1 segment; midline, arrowhead. MNs are color-coded as in Figure 1B.
(C) Posterior (cross-section) view of the neuropil (outlined) and cortex in A1. Note the MN dendrites target the dorsal neuropil.

692 (D) Representative images showing the morphological similarity between MNs identified in vivo by backfills
693 (Mauss et al. 2009) versus the most similar MN reconstruction from the TEM volume. The top section in each
694 panel shows the morphology of the MN dendrites based on in vivo backfills; used with permission); six distinct
695 Fas2 fascicles (three per hemisegment) are shown in white; midline, arrowhead. The bottom section shows MN
696 dendrite morphology reconstructed from the TEM volume in A1.
697
698 **Figure 5. Motor neurons innervating spatial muscle groups or co-activated muscle groups have post-synapses**
699 **in distinct regions of neuropil.**
700 (A) Spatial distributions of post-synaptic sites for MN pools innervating distinct spatial muscle groups (labeled in box).
701 Plots are 1D kernel density estimates for the mediolateral (ML), dorsoventral (DV) and anteroposterior (AP) axes.
702 Arrowheads represent peaks of significantly different distributions (two sample Kolmogorov-Smirnov test; $p<.05$).
703 (B) Hierarchical clustering of MNs by their synapse similarity score reveals MN myotopic organization. To generate a
704 similarity matrix, pairwise synapse similarity scores were generated separately for MNs exiting the left A1 nerve and
705 right A1 nerve. The pairwise similarities for the left and right pools of MNs were highly correlated; $R = .95$. Clustering
706 was performed on the average of the left and right similarity matrices.
707 (C) Density estimates of the post-synaptic sites for MN pool innervating forward co-active muscle groups (labeled in
708 box). Arrowheads represent peaks of significantly different distributions (two sample Kolmogorov-Smirnov test;
709 $p<.05$)
710 (D) Spatial distribution of post-synapse locations for MN18 (red) vs remaining transverse muscles (black) shows MN18
711 has more posterior distribution of post-synapses compared to the remaining neurons in the same spatial muscle group.
712 (E) Spatial distribution of post-synapse locations for MN2 (red) versus remaining dorsal longitudinal muscles (black)
713 shows no difference in spatial distribution compared to the remaining neurons in the same spatial muscle group.
714
715 **Figure 6**. **Identification of 118 premotor neurons at synapse-level in the EM reconstruction**.
716 (A) Dorsal view centered on the A1 segment showing all 118 pair of PMNs reconstructed in this study.
717 (B) Posterior (cross-section) view of the PMN pre-synapse location (red) and post-synapse location (cyan) within
718 the A1 neuropil. Density plots shown for the dorsoventral axis (left) and mediolateral axis (bottom). Dorsal, up.
719 (C) Dorsal view of entire larval neuropil to show anteroposterior distribution of pre-synapse (red) and post-
720 synapse (cyan) location. Density plots shown for the anteroposterior axis (bottom).
721 (D-G) Quantification of PMN-MN connectivity. All A1 MNs, A2 MN-25, and 118 pair of PMNs were used to
722 generate these histograms. (D) PMNs innervate an average of 8 MNs. X-axis shows binned number of MNs
723 receiving inputs from PMNs. Y-axis shows number of PMNs in each bin (D') Swarm-violin plot representation of
724 the same dataset used in D. (E) MNs receive inputs from an average of 32.5 PMNs from this population of
725 PMNs. X-axis shows binned number of PMNs providing output to MNs. Y-axis shows number of MNs in each
726 bin. (E') Swarm-violin plot representation of the same dataset used in E. (F) Histogram showing binned fraction
727 of PMN output to MNs. Y-axis shows number of PMNs in each bin. (F') Swarm-violin plot representation of the
728 same dataset used in F. (G) Histogram showing binned fraction of MN inputs from PMNs. Y-axis shows number
729 of MNs in each bin. 76% of total MN post-synapses receive input from the 118 PMNs. (G') Swarm-violin plot
730 representation of the same dataset used in G.
731 (H-J) Quantification of PMN morphology.
732
733 **Figure 7. PMN pools preferentially connected to individual spatial muscle groups and co-activated**
734 **muscle groups.**
735 (A,B,D) Hierarchical clustering of PMNs based on their connectivity to MNs of the same spatial muscle group
736 (A), forward co-activated muscle group (B), or backward co-activated muscle group (D). The data were
737 standardized within the rows, with maximum assigned 1.0 and other row values relative to that maximum value.
738 Heat maps represent the mean of normalized weighted-synaptic output of a given left/right pair of PMNs onto
739 left/right pair of MNs grouped in each panel. (A) Pools of PMNs show enriched connectivity to spatial muscle
740 groups (dark blue). (B) Pools of PMNs show enriched connectivity to F1-F4 co-activated muscle groups (dark
741 blue); arrow, A27h. (D) Pools of PMNs show enriched connectivity to B1-B4 co-activated muscle groups (dark
742 blue).
743 (C) Dual color calcium imaging of jRCaMP1b in A27h (red) and GCaMP6m in U1-U5 MNs (black).

Consistent with predictions from the connectome, U1-U5 MNs (co-activated muscle group F1/2) are activated before A27h (co-activated muscle group F3) during forward locomotion. Red and dark error bars (ribbons) represent the standard deviation of the average neuronal activity. Genotype: *CQ-lexA/+; lexAop-GCaMP6m/R36G02-Gal4 UAS-jRCaMP1b.*

Figure 8. Neuronal asymmetry along the anterior-posterior axis may contribute to differences seen between forward and backward co-activated muscle groups. (A) MN18 has asymmetric posterior dendrites that could be activated earlier during forward locomotion than during backward locomotion. (B) MN25 has asymmetric anterior dendrites that could be activated earlier during backward locomotion than during forward locomotion. (C) PMN A02i has an asymmetric anterior axon that could inhibit target MNs earlier during forward locomotion than during backward locomotion. (D) PMN A03a4 has an asymmetric anterior axon that could excite target MNs earlier during forward locomotion than during backward locomotion.
(E, F) Both PMN A03a5and A01j have asymmetric posterior axon that could induce target MNs earlier during backward locomotion than during forward locomotion.

Figure 9. **Recurrent network model generating sequential MN activity.**
(A) The PMN and MN network of the A1 and A2 segments was modeled using connectivity taken from the EM reconstruction. Connections within each segment (light gray circles) are identical. The network was optimized using gradient descent to produce a sequential pattern of activity in the MNs (MNs) when a tonic external command input for forward (forward, black) or backward (backward, red) locomotion was applied.
(B) The network in A was optimized to produce an appropriate sequential activity pattern of co-activated muscle groups during forward and backward crawling. The direction of propagation from the posterior (A2) to anterior (A1) segment or vice versa differs for forward and backward crawling. To compare PMN activity relative to MN activation, time is measured in units normalized to the onset and offset of MN activity in a segment (bottom right).
(C) Y-Axis is the normalized activity of a subset of PMNs in the model during forward and backward crawling. Thick lines denote averages over the ensemble of models generated. X-axis (time) is measured relative to A1 MN onset and offset as in B. Arrowheads denote the peak activation onset time for the MNs innervating different co-activated muscle groups (color key as in panel B); exc, excitatory; inh, inhibitory.

Figure 10. Calcium imaging of A31k/A06l/A23a PMNs and their target MNs validates the activity pattern predicted by recurrent modeling.
(A-B) Dual color calcium imaging of jRCaMP1b in A31k (red) and GCaMP6m in MNs (black).
Consistent with the recurrent model predictions, A31k fires with a delay after its post-synaptic MNs in both forward (A) and backward (B) waves. Red and dark error bars (ribbons) represent the standard deviation of the average neuronal activity. Genotype: *CQ-lexA/+; lexAop-GCaMP6m/R87H09-Gal4 UAS-jRCaMP1b.*
(C-D) Single color calcium imaging of jRCaMP1b in A31k (red) and A06l (black). Consistent with the recurrent model predictions, A31k and A06l show synchronous activity patterns during forward (C) and backward waves (D). Red and dark error bars (ribbons) represent the standard deviation of the average neuronal activity.
Genotype: *R87H09-Gal4 UAS-jRCaMP1b.*
(E) A23a fires later during forward locomotion than during backward locomotion. Dual color calcium imaging of jRCaMP1b in A23a (red) and GCaMP6m in MNs (black). Red and dark error bars (ribbons) represent the standard deviation of the average neuronal activity. Genotype: *CQ-lexA/+; lexAop-GCaMP6m/R78F07-Gal4 UAS-jRCaMP1b.*

Figure 11. Neural circuit motifs specific for forward or backward locomotion.
Circuit motifs composed of forward-specific PMNs (A-C) and backward specific PMNs (D-E). See text for details. Arrow/green, excitatory connection; T-bar/red, inhibitory connection; F1-F4, forward co-active group; B1-B4, backward co-active group.

References

Arber S. 2017. Organization and function of neuronal circuits controlling movement. *EMBO molecular medicine* **9**: 281-284.

Arber S, Costa RM. 2018. Connecting neuronal circuits for movement. *Science (New York, NY)* **360**: 1403-1404.

Bagnall MW, McLean DL. 2014. Modular organization of axial microcircuits in zebrafish. *Science (New York, NY)* **343**: 197-200.

Bargmann CI, Marder E. 2013. From the connectome to brain function. *Nature methods* **10**: 483-490.

Bate M. 1990. The embryonic development of larval muscles in Drosophila. *Development (Cambridge, England)* **110**: 791-804.

Berni J, Pulver SR, Griffith LC, Bate M. 2012. Autonomous circuitry for substrate exploration in freely moving Drosophila larvae. *Current biology : CB* **22**: 1861-1870.

Bikoff JB, Gabitto MI, Rivard AF, Drobac E, Machado TA, Miri A, Brenner-Morton S, Famojure E, Diaz C, Alvarez FJ et al. 2016. Spinal Inhibitory Interneuron Diversity Delineates Variant Motor Microcircuits. *Cell* **165**: 207-219.

Brenner S. 2010. Sequences and consequences. *Philosophical transactions of the Royal Society of London Series B, Biological sciences* **365**: 207-212.

Briggman KL, Kristan WB. 2008. Multifunctional pattern-generating circuits. *Annual review of neuroscience* **31**: 271-294.

Briggman KL, Kristan WB, Jr. 2006. Imaging dedicated and multifunctional neural circuits generating distinct behaviors. *The Journal of neuroscience : the official journal of the Society for Neuroscience* **26**: 10925-10933.

Brodfuehrer PD, Thorogood MS. 2001. Identified neurons and leech swimming behavior. *Progress in neurobiology* **63**: 371-381.

Bucher D, Taylor AL, Marder E. 2006. Central pattern generating neurons simultaneously express fast and slow rhythmic activities in the stomatogastric ganglion. *Journal of neurophysiology* **95**: 3617-3632.

Burgos A, Honjo K, Ohyama T, Qian CS, Shin GJ, Gohl DM, Silies M, Tracey WD, Zlatic M, Cardona A et al. 2018. Nociceptive interneurons control modular motor pathways to promote escape behavior in Drosophila. *eLife* **7**.

Butler VJ, Branicky R, Yemini E, Liewald JF, Gottschalk A, Kerr RA, Chklovskii DB, Schafer WR. 2015. A consistent muscle activation strategy underlies crawling and swimming in Caenorhabditis elegans. *Journal of the Royal Society, Interface* **12**: 20140963.

Carreira-Rosario A, Zarin AA, Clark MQ, Manning L, Fetter RD, Cardona A, Doe CQ. 2018. MDN brain descending neurons coordinately activate backward and inhibit forward locomotion. *eLife* **7**.

Choi JC, Park D, Griffith LC. 2004. Electrophysiological and morphological characterization of identified motor neurons in the Drosophila third instar larva central nervous system. *Journal of neurophysiology* **91**: 2353-2365.

Clark MQ, Zarin AA, Carreira-Rosario A, Doe CQ. 2018. Neural circuits driving larval locomotion in Drosophila. *Neural development* **13**: 6.

Crisp S, Evers JF, Fiala A, Bate M. 2008. The development of motor coordination in Drosophila embryos. *Development (Cambridge, England)* **135**: 3707-3717.

Crone SA, Quinlan KA, Zagoraiou L, Droho S, Restrepo CE, Lundfald L, Endo T, Setlak J, Jessell TM, Kiehn O et al. 2008. Genetic ablation of V2a ipsilateral interneurons disrupts left-right locomotor coordination in mammalian spinal cord. *Neuron* **60**: 70-83.

Crossley A. 1978. The morphology and development of the Drosophila muscular system. in *The Genetics and Biology of Drosophila*, pp. 499-560. Academic Press, London, New York, and San Francisco.

de Castro C, Titlow J, Majeed ZR, Cooper RL. 2014. Analysis of various physiological salines for heart rate, CNS function, and synaptic transmission at neuromuscular junctions in Drosophila melanogaster larvae. *Journal of comparative physiology A, Neuroethology, sensory, neural, and behavioral physiology* **200**: 83-92.

Dixit R, Vijayraghavan K, Bate M. 2008. Hox genes and the regulation of movement in Drosophila. *Developmental neurobiology* **68**: 309-316.

Dougherty KJ, Zagoraiou L, Satoh D, Rozani I, Doobar S, Arber S, Jessell TM, Kiehn O. 2013. Locomotor rhythm generation linked to the output of spinal shox2 excitatory interneurons. *Neuron* **80**: 920-933.

Eichler K, Li F, Litwin-Kumar A, Park Y, Andrade I, Schneider-Mizell CM, Saumweber T, Huser A, Eschbach C, Gerber B et al. 2017. The complete connectome of a learning and memory centre in an insect brain. *Nature* **548**: 175-182.

Eklof-Ljunggren E, Haupt S, Ausborn J, Dehnisch I, Uhlen P, Higashijima S, El Manira A. 2012. Origin of excitation underlying locomotion in the spinal circuit of zebrafish. *Proceedings of the National Academy of Sciences of the United States of America* **109**: 5511-5516.

Fogarty MJ, Mantilla CB, Sieck GC. 2018. Breathing: Motor Control of Diaphragm Muscle. *Physiology (Bethesda, Md)* **33**: 113-126.

Fushiki A, Zwart MF, Kohsaka H, Fetter RD, Cardona A, Nose A. 2016. A circuit mechanism for the propagation of waves of muscle contraction in Drosophila. *eLife* **5**.

Gjorgjieva J, Berni J, Evers JF, Eglen SJ. 2013. Neural circuits for peristaltic wave propagation in crawling Drosophila larvae: analysis and modeling. *Frontiers in computational neuroscience* **7**: 24.

Goetz C, Pivetta C, Arber S. 2015. Distinct limb and trunk premotor circuits establish laterality in the spinal cord. *Neuron* **85**: 131-144.

Gorczyca M, Augart C, Budnik V. 1993. Insulin-like receptor and insulin-like peptide are localized at neuromuscular junctions in Drosophila. *The Journal of neuroscience : the official journal of the Society for Neuroscience* **13**: 3692-3704.

Grillner S. 2003. The motor infrastructure: from ion channels to neuronal networks. *Nature reviews Neuroscience* **4**: 573-586.

Grillner S, Jessell TM. 2009. Measured motion: searching for simplicity in spinal locomotor networks. *Current opinion in neurobiology* **19**: 572-586.

Hasegawa E, Truman JW, Nose A. 2016. Identification of excitatory premotor interneurons which regulate local muscle contraction during Drosophila larval locomotion. *Scientific reports* **6**: 30806.

Haspel G, Donovan MJ, Hart AC. 2010. Motoneurons Dedicated to Either Forward or Backward Locomotion in the Nematode <em>Caenorhabditis elegans</em&gt. *The Journal of Neuroscience* **30**: 11151.

Heckscher ES, Lockery SR, Doe CQ. 2012. Characterization of Drosophila larval crawling at the level of organism, segment, and somatic body wall musculature. *The Journal of neuroscience : the official journal of the Society for Neuroscience* **32**: 12460-12471.

Heckscher ES, Zarin AA, Faumont S, Clark MQ, Manning L, Fushiki A, Schneider-Mizell CM, Fetter RD, Truman JW, Zwart MF et al. 2015. Even-Skipped(+) Interneurons Are Core Components of a Sensorimotor Circuit that Maintains Left-Right Symmetric Muscle Contraction Amplitude. *Neuron* **88**: 314-329.

Hessinger C, Technau GM, Rogulja-Ortmann A. 2017. The Drosophila Hox gene Ultrabithorax acts in both muscles and motoneurons to orchestrate formation of specific neuromuscular connections. *Development (Cambridge, England)* **144**: 139-150.

Hoang B, Chiba A. 2001. Single-cell analysis of Drosophila larval neuromuscular synapses. *Developmental biology* **229**: 55-70.

Hooper JE. 1986. Homeotic gene function in the muscles of Drosophila larvae. *The EMBO journal* **5**: 2321-2329.

Izquierdo EJ, Beer RD. 2013. Connecting a connectome to behavior: an ensemble of neuroanatomical models of C. elegans klinotaxis. *PLoS computational biology* **9**: e1002890.

Izquierdo EJ, Williams PL, Beer RD. 2015. Information Flow through a Model of the C. elegans Klinotaxis Circuit. *PloS one* **10**: e0140397.

Karbowski J, Schindelman G, Cronin CJ, Seah A, Sternberg PW. 2008. Systems level circuit model of C. elegans undulatory locomotion: mathematical modeling and molecular genetics. *Journal of computational neuroscience* **24**: 253-276.

Kawano T, Po Michelle D, Gao S, Leung G, Ryu William S, Zhen M. 2011. An Imbalancing Act: Gap Junctions Reduce the Backward Motor Circuit Activity to Bias C. elegans for Forward Locomotion. *Neuron* **72**: 572-586.

Kiehn O. 2006. Locomotor circuits in the mammalian spinal cord. *Annual review of neuroscience* **29**: 279-306.

Kimura Y, Satou C, Fujioka S, Shoji W, Umeda K, Ishizuka T, Yawo H, Higashijima S. 2013. Hindbrain V2a neurons in the excitation of spinal locomotor circuits during zebrafish swimming. *Current biology : CB* **23**: 843-849.

Kohsaka H, Guertin PA, Nose A. 2017. Neural Circuits Underlying Fly Larval Locomotion. *Current pharmaceutical design* **23**: 1722-1733.
Kohsaka H, Takasu E, Morimoto T, Nose A. 2014. A group of segmental premotor interneurons regulates the speed of axial locomotion in Drosophila larvae. *Current biology : CB* **24**: 2632-2642.
Kohsaka H, Zwart MF, Fushiki A, Fetter RD, Truman JW, Cardona A, Nose A. 2019. Regulation of forward and backward locomotion through intersegmental feedback circuits in Drosophila larvae. *Nature communications* **10**: 2654.
Koon AC, Ashley J, Barria R, DasGupta S, Brain R, Waddell S, Alkema MJ, Budnik V. 2011. Autoregulatory and paracrine control of synaptic and behavioral plasticity by octopaminergic signaling. *Nature neuroscience* **14**: 190-199.
Koon AC, Budnik V. 2012. Inhibitory control of synaptic and behavioral plasticity by octopaminergic signaling. *The Journal of neuroscience : the official journal of the Society for Neuroscience* **32**: 6312-6322.
Kristan WB, Jr., Calabrese RL, Friesen WO. 2005. Neuronal control of leech behavior. *Progress in neurobiology* **76**: 279-327.
Kunert JM, Maia PD, Kutz JN. 2017. Functionality and Robustness of Injured Connectomic Dynamics in C. elegans: Linking Behavioral Deficits to Neural Circuit Damage. *PLoS computational biology* **13**: e1005261.
Landgraf M, Bossing T, Technau GM, Bate M. 1997. The origin, location, and projections of the embryonic abdominal motorneurons of Drosophila. *The Journal of neuroscience : the official journal of the Society for Neuroscience* **17**: 9642-9655.
Landgraf M, Jeffrey V, Fujioka M, Jaynes JB, Bate M. 2003. Embryonic origins of a motor system: motor dendrites form a myotopic map in Drosophila. *PLoS biology* **1**: E41.
Lemon WC, Pulver SR, Hockendorf B, McDole K, Branson K, Freeman J, Keller PJ. 2015. Whole-central nervous system functional imaging in larval Drosophila. *Nature communications* **6**: 7924.
Lieske SP, Thoby-Brisson M, Telgkamp P, Ramirez JM. 2000. Reconfiguration of the neural network controlling multiple breathing patterns: eupnea, sighs and gasps [see comment]. *Nature neuroscience* **3**: 600-607.
Ljunggren EE, Haupt S, Ausborn J, Ampatzis K, El Manira A. 2014. Optogenetic activation of excitatory premotor interneurons is sufficient to generate coordinated locomotor activity in larval zebrafish. *The Journal of neuroscience : the official journal of the Society for Neuroscience* **34**: 134-139.
Loveless J, Lagogiannis K, Webb B. 2018. Mechanics of exploration in Drosophila melanogaster. *bioRxiv*: 354795.
MacNamee SE, Liu KE, Gerhard S, Tran CT, Fetter RD, Cardona A, Tolbert LP, Oland LA. 2016. Astrocytic glutamate transport regulates a Drosophila CNS synapse that lacks astrocyte ensheathment. *The Journal of comparative neurology* **524**: 1979-1998.
Macosko EZ, Pokala N, Feinberg EH, Chalasani SH, Butcher RA, Clardy J, Bargmann CI. 2009. A hub-and-spoke circuit drives pheromone attraction and social behaviour in C. elegans. *Nature* **458**: 1171-1175.
Marder E, Bucher D. 2001. Central pattern generators and the control of rhythmic movements. *Current biology : CB* **11**: R986-996.
Marin-Burgin A, Kristan WB, Jr., French KA. 2008. From synapses to behavior: development of a sensory-motor circuit in the leech. *Developmental neurobiology* **68**: 779-787.
Mauss A, Tripodi M, Evers JF, Landgraf M. 2009. Midline signalling systems direct the formation of a neural map by dendritic targeting in the Drosophila motor system. *PLoS biology* **7**: e1000200.
Mullins OJ, Hackett JT, Buchanan JT, Friesen WO. 2011. Neuronal control of swimming behavior: comparison of vertebrate and invertebrate model systems. *Progress in neurobiology* **93**: 244-269.
Mulloney B, Smarandache-Wellmann C. 2012. Neurobiology of the crustacean swimmeret system. *Progress in neurobiology* **96**: 242-267.
Mulloney B, Smarandache-Wellmann C, Weller C, Hall WM, DiCaprio RA. 2014. Proprioceptive feedback modulates coordinating information in a system of segmentally distributed microcircuits. *Journal of neurophysiology* **112**: 2799-2809.
Nern A, Pfeiffer BD, Rubin GM. 2015. Optimized tools for multicolor stochastic labeling reveal diverse stereotyped cell arrangements in the fly visual system. *Proceedings of the National Academy of Sciences of the United States of America* **112**: E2967-2976.
Nishimaru H, Kakizaki M. 2009. The role of inhibitory neurotransmission in locomotor circuits of the developing mammalian spinal cord. *Acta physiologica (Oxford, England)* **197**: 83-97.

Ohyama T, Schneider-Mizell CM, Fetter RD, Aleman JV, Franconville R, Rivera-Alba M, Mensh BD, Branson KM, Simpson JH, Truman JW et al. 2015. A multilevel multimodal circuit enhances action selection in Drosophila. *Nature* **520**: 633-639.

Pearson KG. 1976. Nerve cells without action potentials. in *Comparative neurobiology: modes of communcation in the nervous system* (ed. JC Fentress), pp. 99-110. Sinauer, Sunderland, MA.

Pehlevan C, Paoletti P, Mahadevan L. 2016. Integrative neuromechanics of crawling in D. melanogaster larvae. *eLife* **5**: e11031.

Pierce-Shimomura JT, Chen BL, Mun JJ, Ho R, Sarkis R, McIntire SL. 2008. Genetic analysis of crawling and swimming locomotory patterns in C. elegans. *Proceedings of the National Academy of Sciences of the United States of America* **105**: 20982-20987.

Piggott Beverly J, Liu J, Feng Z, Wescott Seth A, Xu XZS. 2011. The Neural Circuits and Synaptic Mechanisms Underlying Motor Initiation in C. elegans. *Cell* **147**: 922-933.

Popescu IR, Frost WN. 2002. Highly dissimilar behaviors mediated by a multifunctional network in the marine mollusk Tritonia diomedea. *The Journal of neuroscience : the official journal of the Society for Neuroscience* **22**: 1985-1993.

Prinz AA, Bucher D, Marder E. 2004. Similar network activity from disparate circuit parameters. *Nature neuroscience* **7**: 1345-1352.

Pulver SR, Bayley TG, Taylor AL, Berni J, Bate M, Hedwig B. 2015. Imaging fictive locomotor patterns in larval Drosophila. *Journal of neurophysiology* **114**: 2564-2577.

Rakowski F, Karbowski J. 2017. Optimal synaptic signaling connectome for locomotory behavior in Caenorhabditis elegans: Design minimizing energy cost. *PLoS computational biology* **13**: e1005834.

Ramirez JM, Pearson KG. 1988. Generation of motor patterns for walking and flight in motoneurons supplying bifunctional muscles in the locust. *Journal of neurobiology* **19**: 257-282.

Roberts A, Li WC, Soffe SR. 2010. How neurons generate behavior in a hatchling amphibian tadpole: an outline. *Frontiers in behavioral neuroscience* **4**: 16.

Roberts A, Li WC, Soffe SR, Wolf E. 2008. Origin of excitatory drive to a spinal locomotor network. *Brain research reviews* **57**: 22-28.

Roberts WM, Augustine SB, Lawton KJ, Lindsay TH, Thiele TR, Izquierdo EJ, Faumont S, Lindsay RA, Britton MC, Pokala N et al. 2016. A stochastic neuronal model predicts random search behaviors at multiple spatial scales in C. elegans. *eLife* **5**.

Saalfeld S, Cardona A, Hartenstein V, Tomancak P. 2009. CATMAID: collaborative annotation toolkit for massive amounts of image data. *Bioinformatics (Oxford, England)* **25**: 1984-1986.

Schlegel P, Texada MJ, Miroschnikow A, Schoofs A, Huckesfeld S, Peters M, Schneider-Mizell CM, Lacin H, Li F, Fetter RD et al. 2016. Synaptic transmission parallels neuromodulation in a central food-intake circuit. *eLife* **5**.

Schneider-Mizell CM, Gerhard S, Longair M, Kazimiers T, Li F, Zwart MF, Champion A, Midgley FM, Fetter RD, Saalfeld S et al. 2016. Quantitative neuroanatomy for connectomics in Drosophila. *eLife* **5**.

Song J, Ampatzis K, Bjornfors ER, El Manira A. 2016. Motor neurons control locomotor circuit function retrogradely via gap junctions. *Nature* **529**: 399-402.

Takagi S, Cocanougher BT, Niki S, Miyamoto D, Kohsaka H, Kazama H, Fetter RD, Truman JW, Zlatic M, Cardona A et al. 2017. Divergent Connectivity of Homologous Command-like Neurons Mediates Segment-Specific Touch Responses in Drosophila. *Neuron* **96**: 1373-1387.e1376.

Takemura SY, Bharioke A, Lu Z, Nern A, Vitaladevuni S, Rivlin PK, Katz WT, Olbris DJ, Plaza SM, Winston P et al. 2013. A visual motion detection circuit suggested by Drosophila connectomics. *Nature* **500**: 175-181.

Tsalik EL, Hobert O. 2003. Functional mapping of neurons that control locomotory behavior in Caenorhabditis elegans. *Journal of neurobiology* **56**: 178-197.

Tschopp F, Reiser M, Turaga S. 2018. A Connectome Based Hexagonal Lattice Convolutional Network Model of the Drosophila Visual System. *https://arxivorg/abs/180604793v2*.

Vidal-Gadea A, Topper S, Young L, Crisp A, Kressin L, Elbel E, Maples T, Brauner M, Erbguth K, Axelrod A et al. 2011. Caenorhabditis elegans selects distinct crawling and swimming gaits via dopamine and serotonin. *Proceedings of the National Academy of Sciences of the United States of America* **108**: 17504-17509.

Wakabayashi T, Kitagawa I, Shingai R. 2004. Neurons regulating the duration of forward locomotion in Caenorhabditis elegans. *Neuroscience Research* **50**: 103-111.
Wen Q, Po MD, Hulme E, Chen S, Liu X, Kwok SW, Gershow M, Leifer AM, Butler V, Fang-Yen C et al. 2012a. Proprioceptive coupling within motor neurons drives C. elegans forward locomotion. *Neuron* **76**: 750-761.
Wen Q, Po MD, Hulme E, Chen S, Liu X, Kwok Sen W, Gershow M, Leifer Andrew M, Butler V, Fang-Yen C et al. 2012b. Proprioceptive Coupling within Motor Neurons Drives C. elegans Forward Locomotion. *Neuron* **76**: 750-761.
White JG, Southgate E, Thomson JN, Brenner S. 1986. The structure of the nervous system of the nematode Caenorhabditis elegans. *Philosophical transactions of the Royal Society of London Series B, Biological sciences* **314**: 1-340.
Yoshino J, Morikawa RK, Hasegawa E, Emoto K. 2017. Neural Circuitry that Evokes Escape Behavior upon Activation of Nociceptive Sensory Neurons in Drosophila Larvae. *Current biology : CB* **27**: 2499-2504.e2493.
Zagoraiou L, Akay T, Martin JF, Brownstone RM, Jessell TM, Miles GB. 2009. A cluster of cholinergic premotor interneurons modulates mouse locomotor activity. *Neuron* **64**: 645-662.
Zarin AA, Labrador JP. 2017. Motor axon guidance in Drosophila. *Seminars in cell & developmental biology*.
Zhen M, Samuel ADT. 2015. C. elegans locomotion: small circuits, complex functions. *Current opinion in neurobiology* **33**: 117-126.
Zwart MF, Pulver SR, Truman JW, Fushiki A, Fetter RD, Cardona A, Landgraf M. 2016. Selective Inhibition Mediates the Sequential Recruitment of Motor Pools. *Neuron* **91**: 615-628.

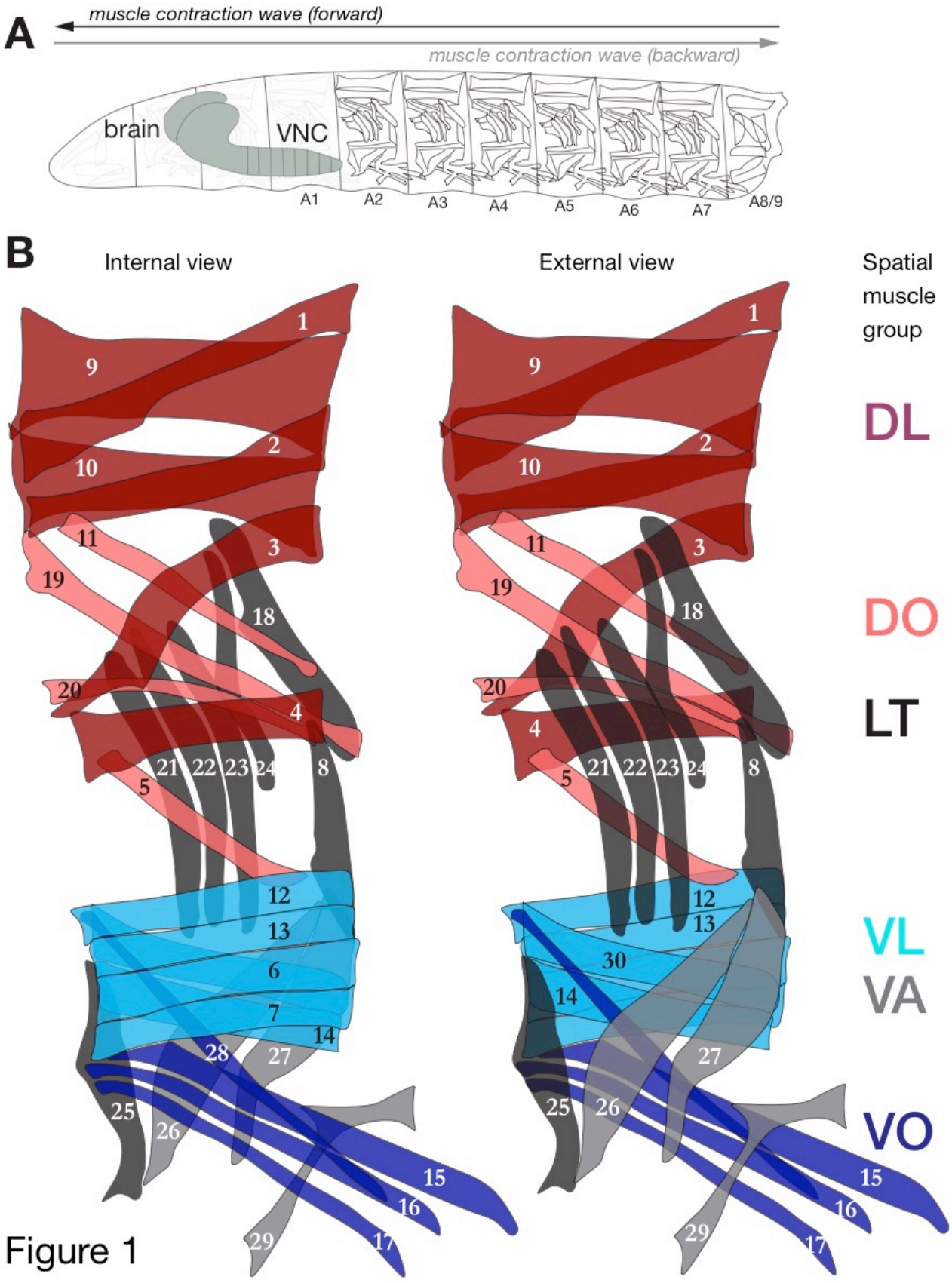

Figure 1

1023

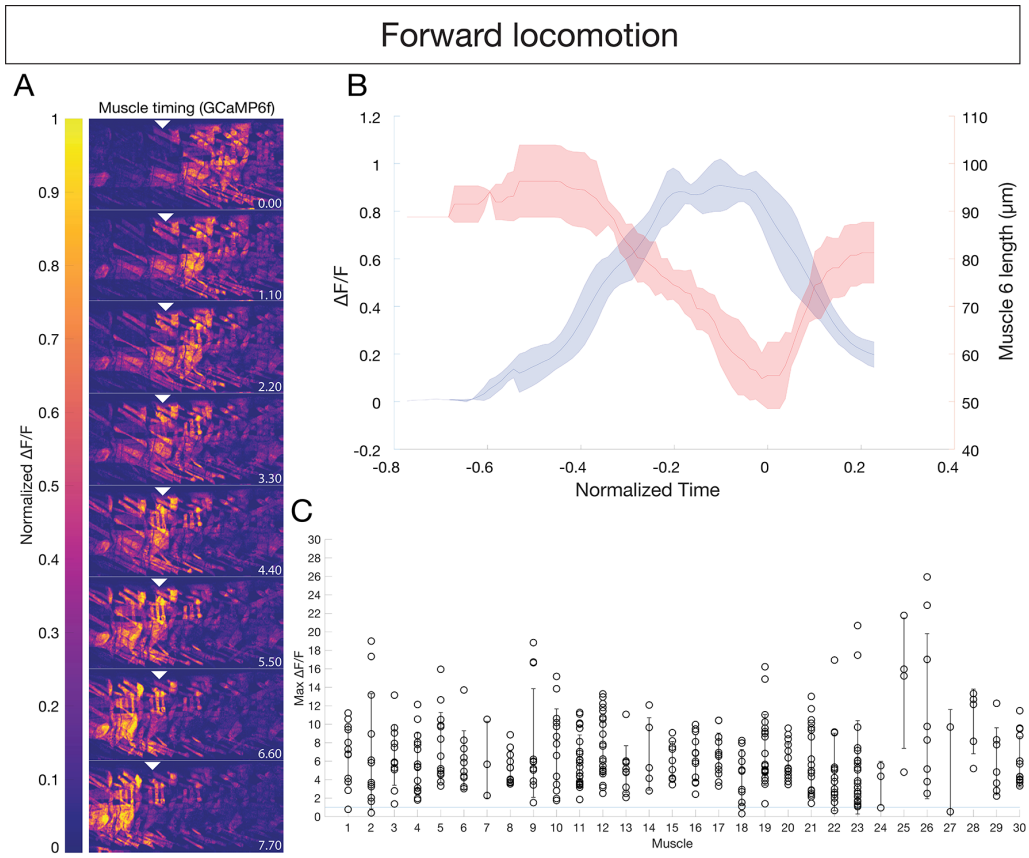

Figure 2

1024

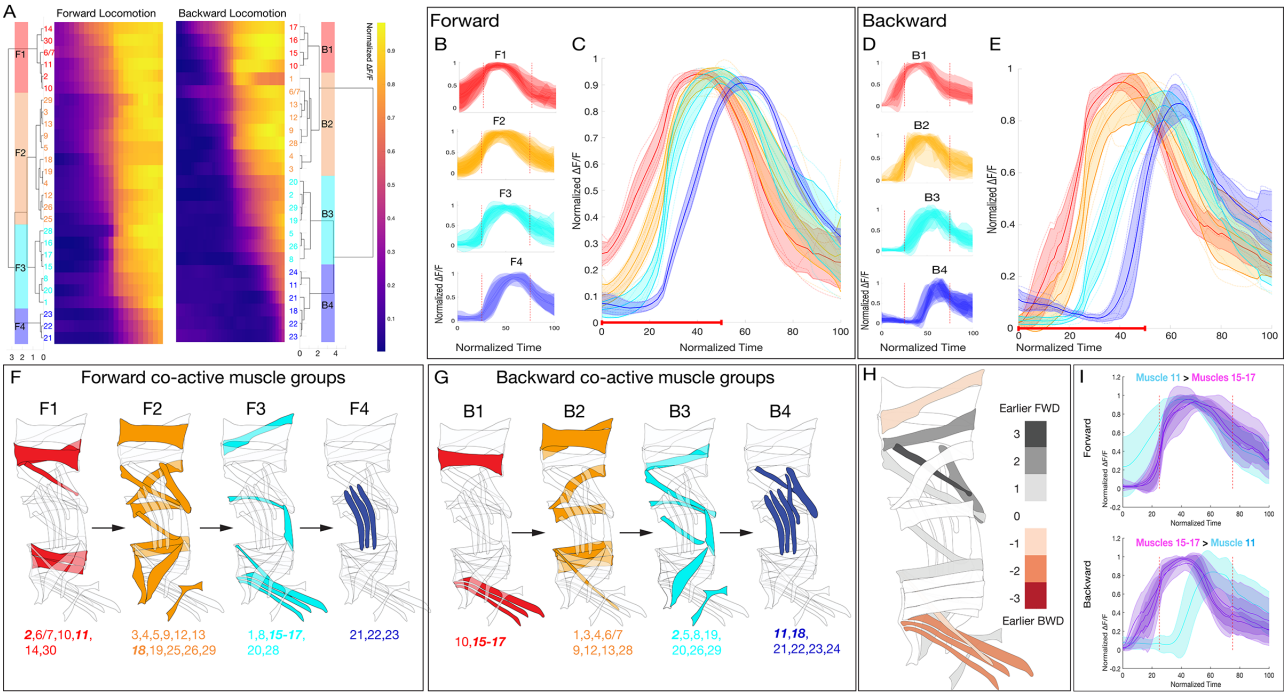
A
Forward Locomotion
Backward Locomotion
F1
F2
F3
F4
B1
B2
B3
B4
Normalized ΔF/F
Forward
B
C
Normalized ΔF/F
Normalized Time
Backward
D
E
F
Forward co-active muscle groups
2,6/7,10,11,
14,30
3,4,5,9,12,13
18,19,25,26,29
1,8,15-17,
20,28
21,22,23
G
Backward co-active muscle groups
10,15-17
1,3,4,6/7
9,12,13,28
2,5,8,19,
20,26,29
11,18,
21,22,23,24
H
Earlier FWD
Earlier BWD
I
Muscle 11 > Muscles 15-17
Muscles 15-17 > Muscle 11
Forward
Backward

Figure 3

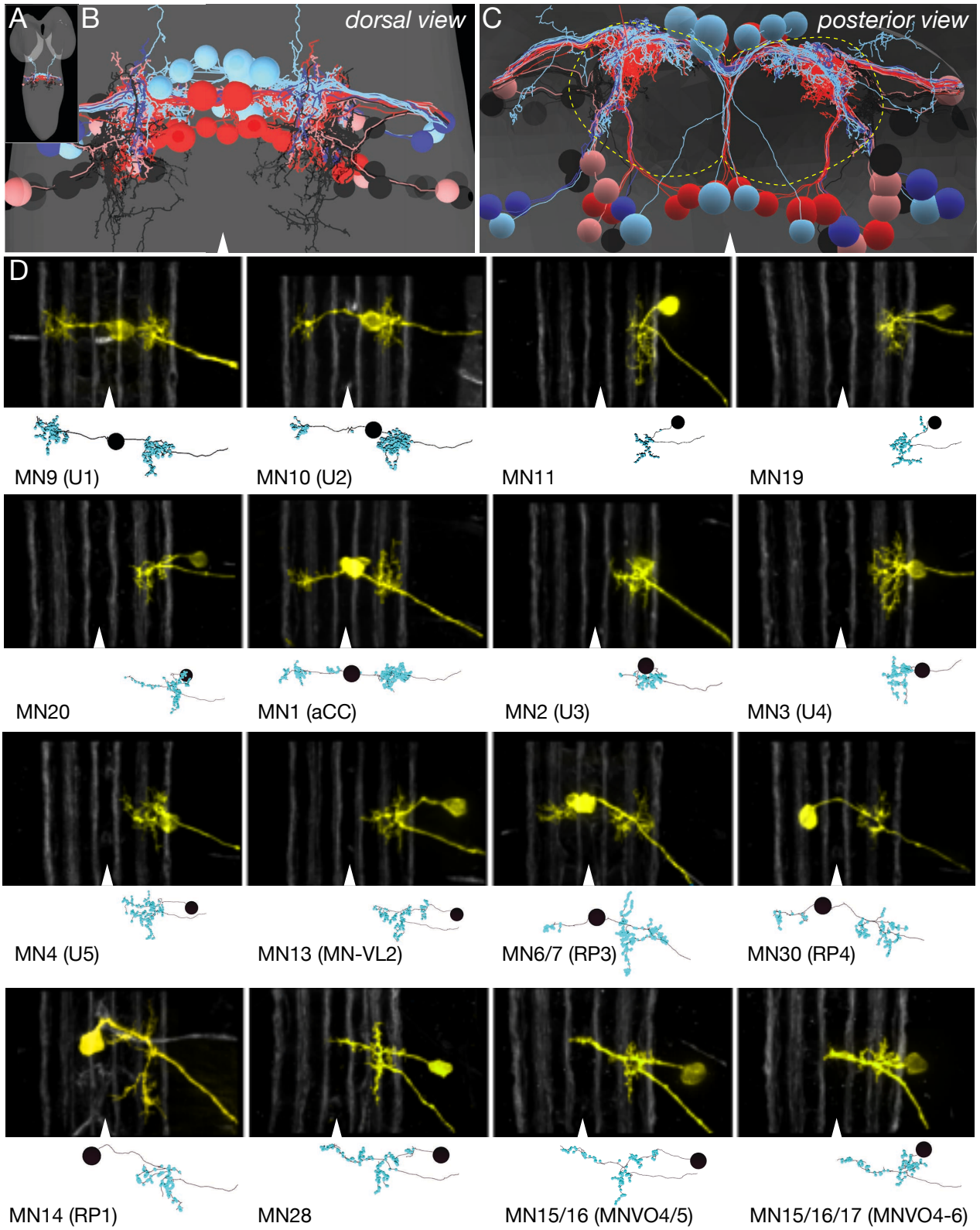
A
B
dorsal view
C
posterior view
D
MN9 (U1)
MN10 (U2)
MN11
MN19
MN20
MN1 (aCC)
MN2 (U3)
MN3 (U4)
MN4 (U5)
MN13 (MN-VL2)
MN6/7 (RP3)
MN30 (RP4)
MN14 (RP1)
MN28
MN15/16 (MNVO4/5)
MN15/16/17 (MNVO4-6)

Figure 4

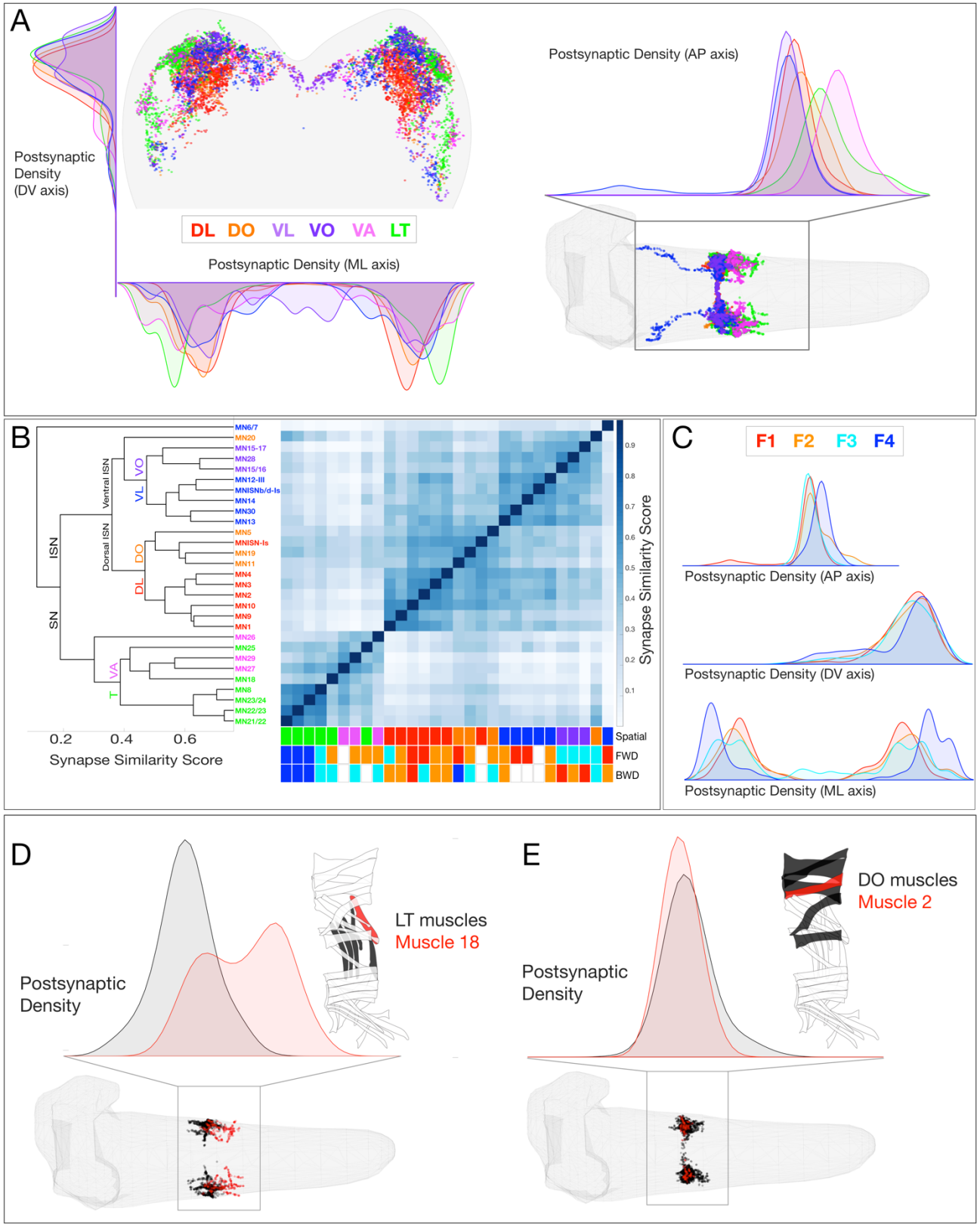

Figure 5

1028

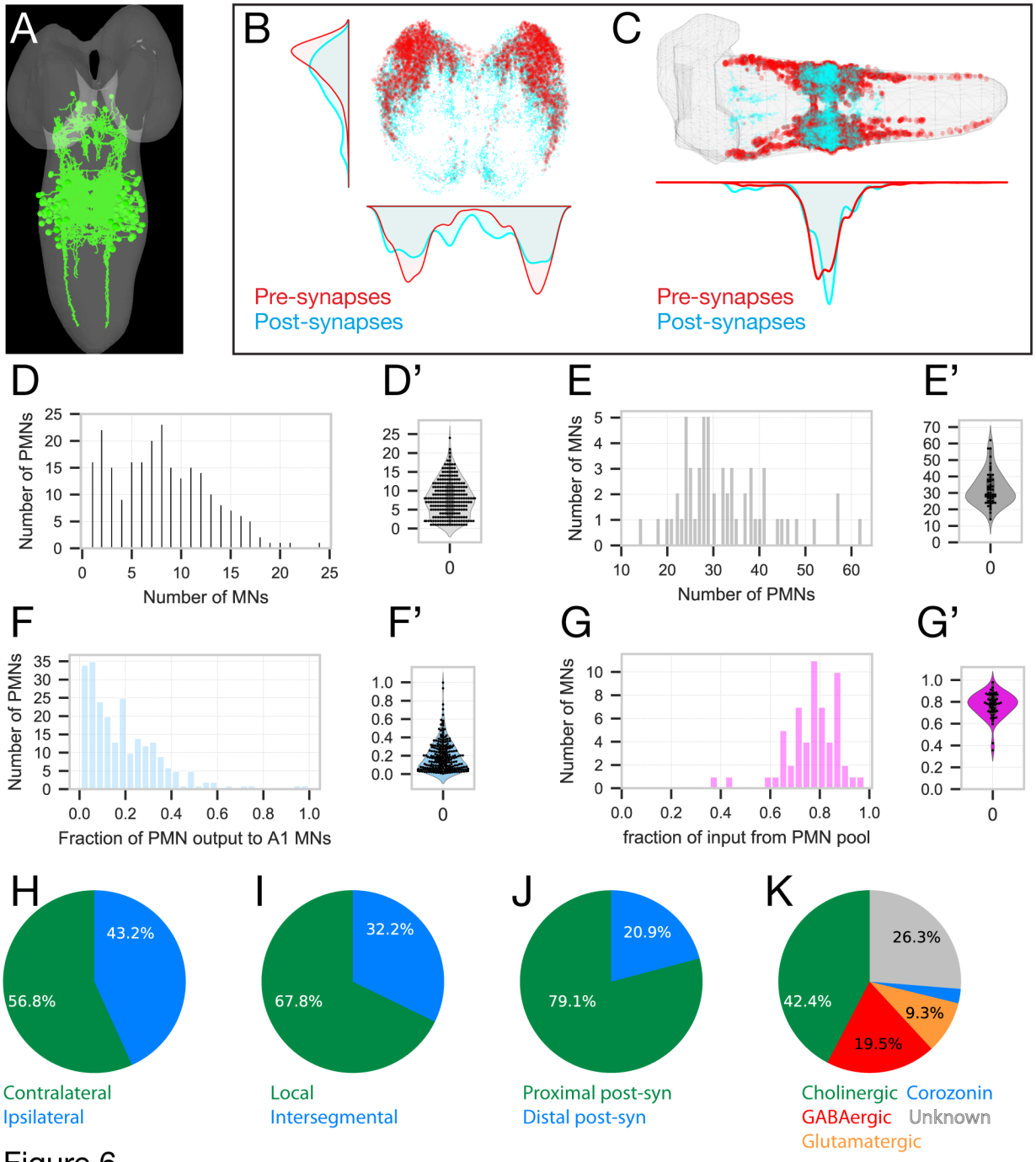

Figure 6

1029

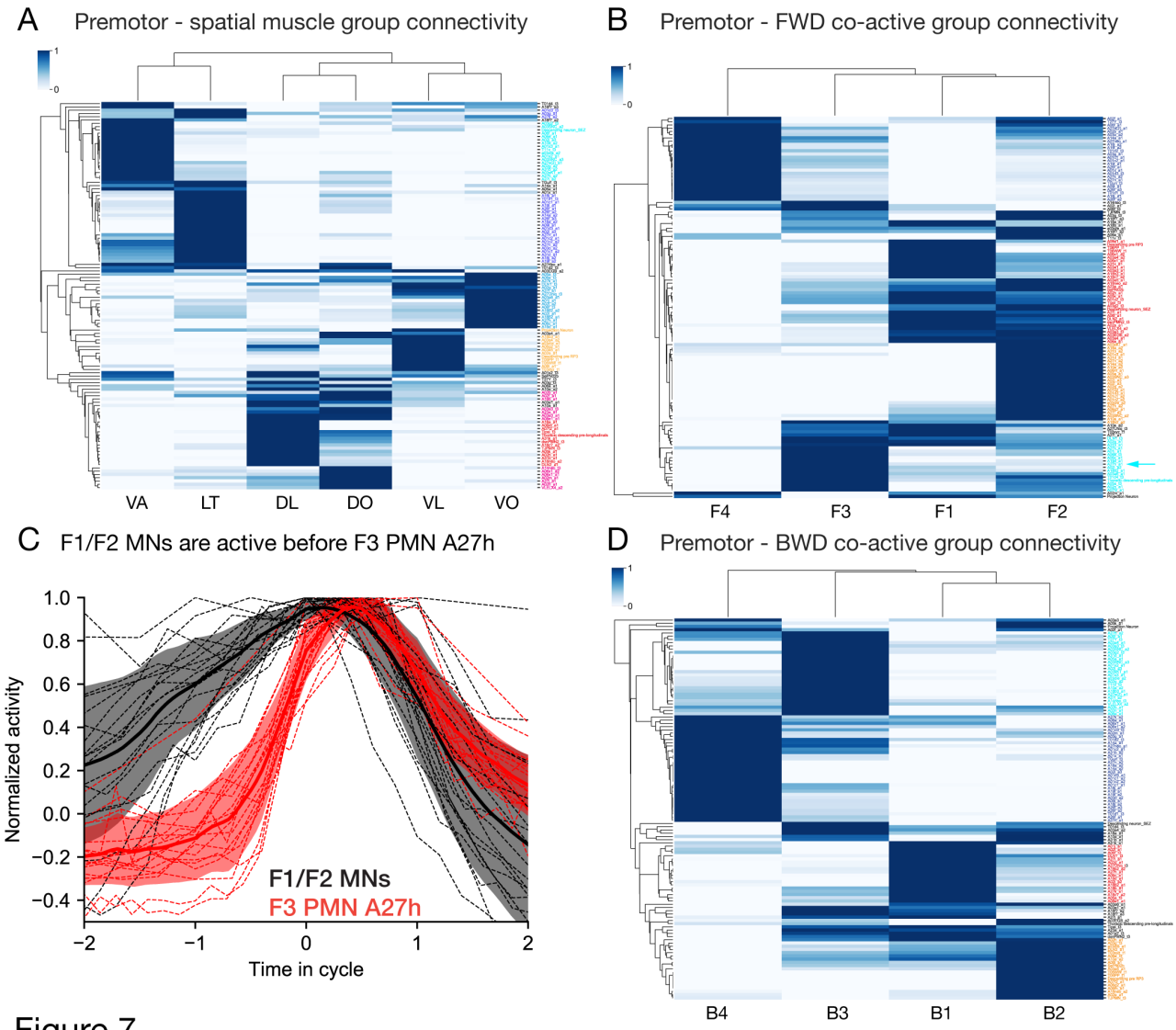

Figure 7

1030

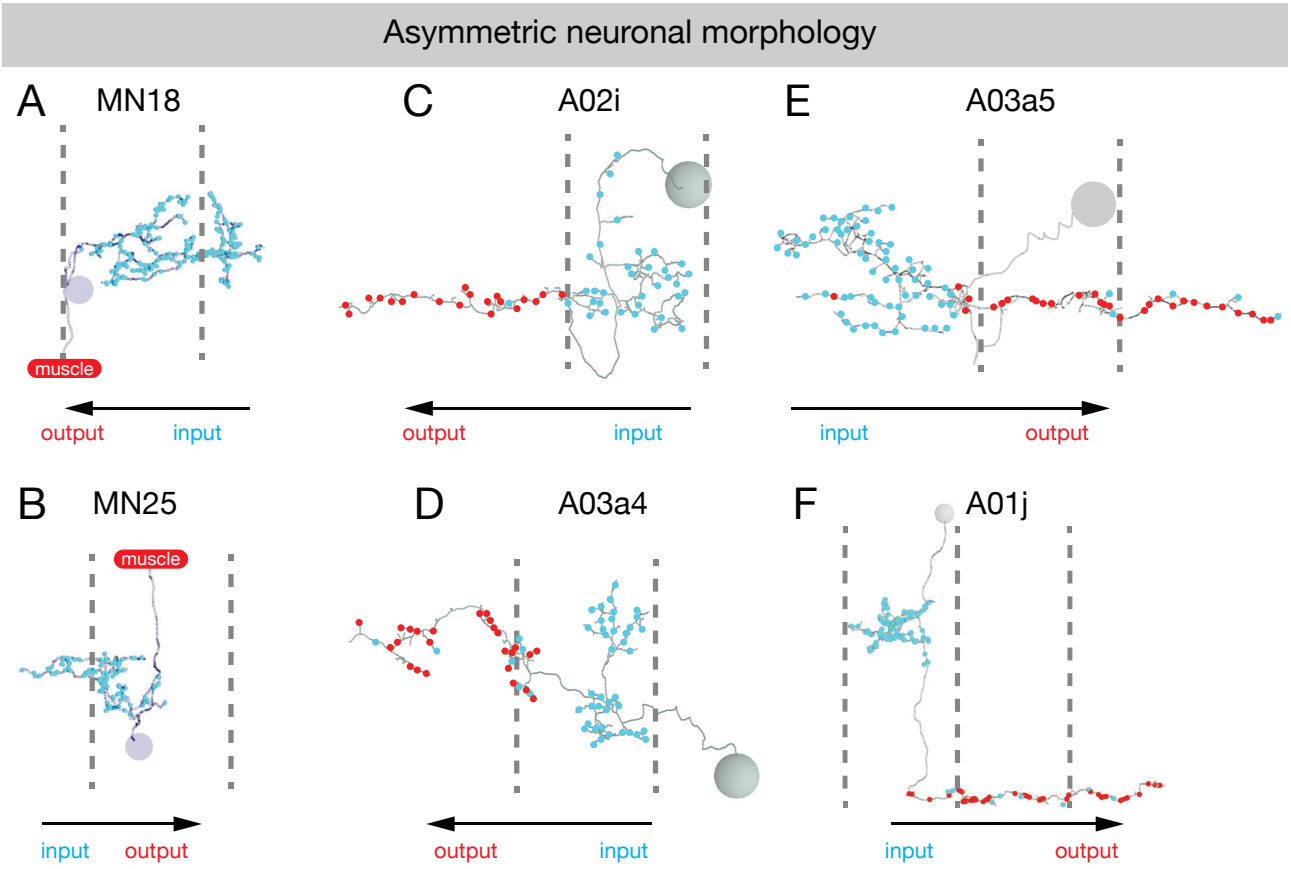

Figure 8

1031

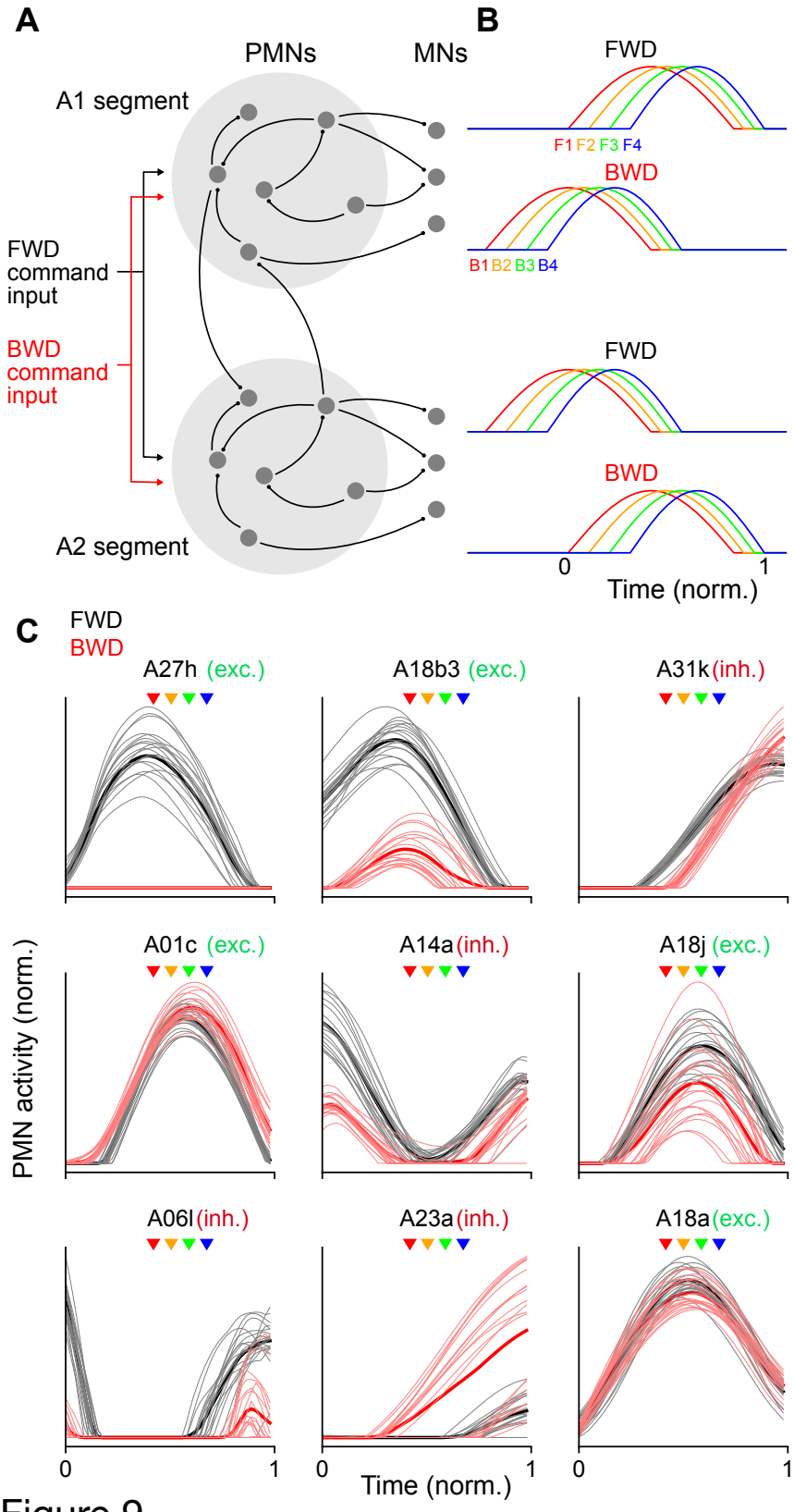

Figure 9

1032

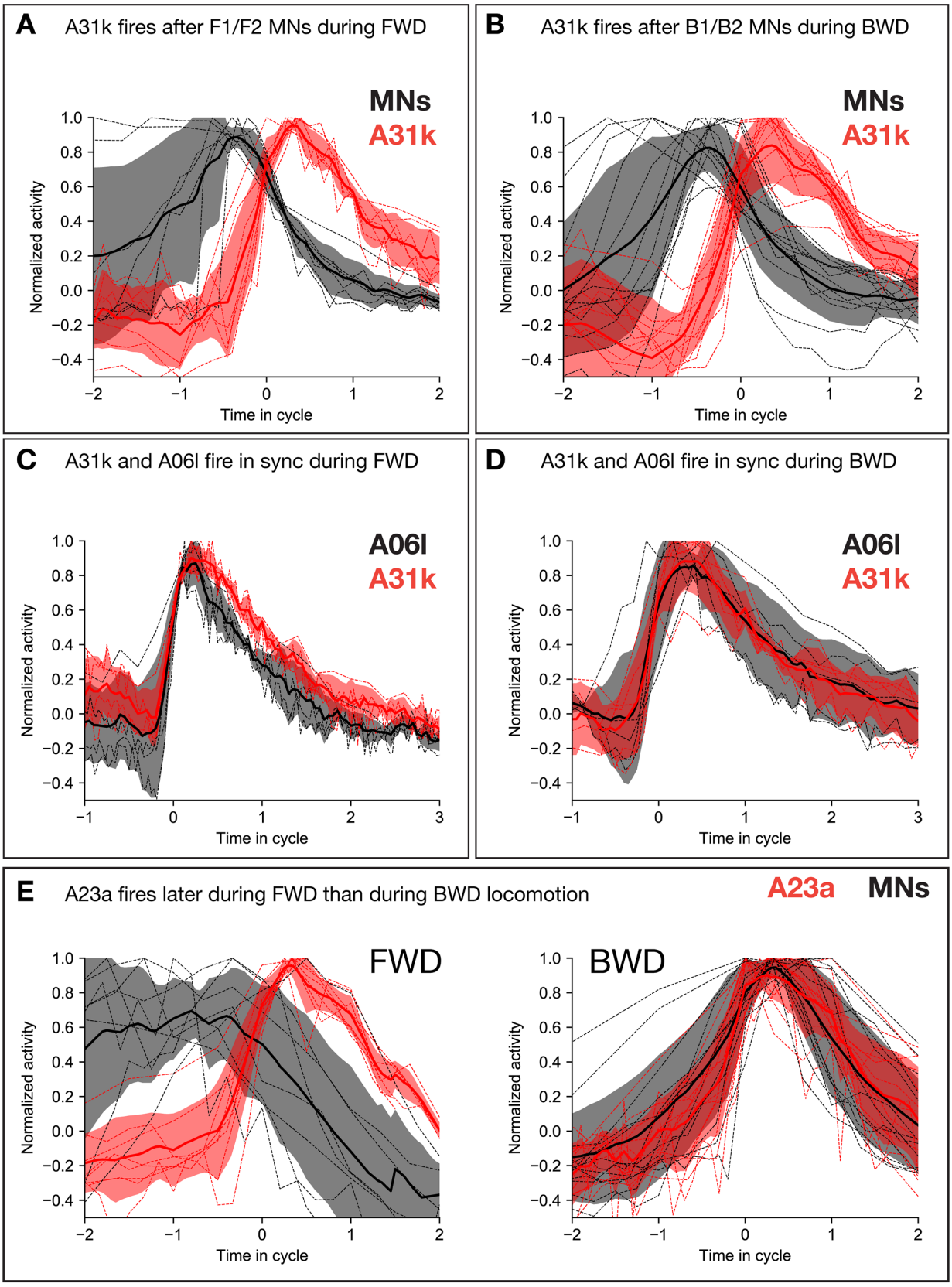

Figure 10

1033

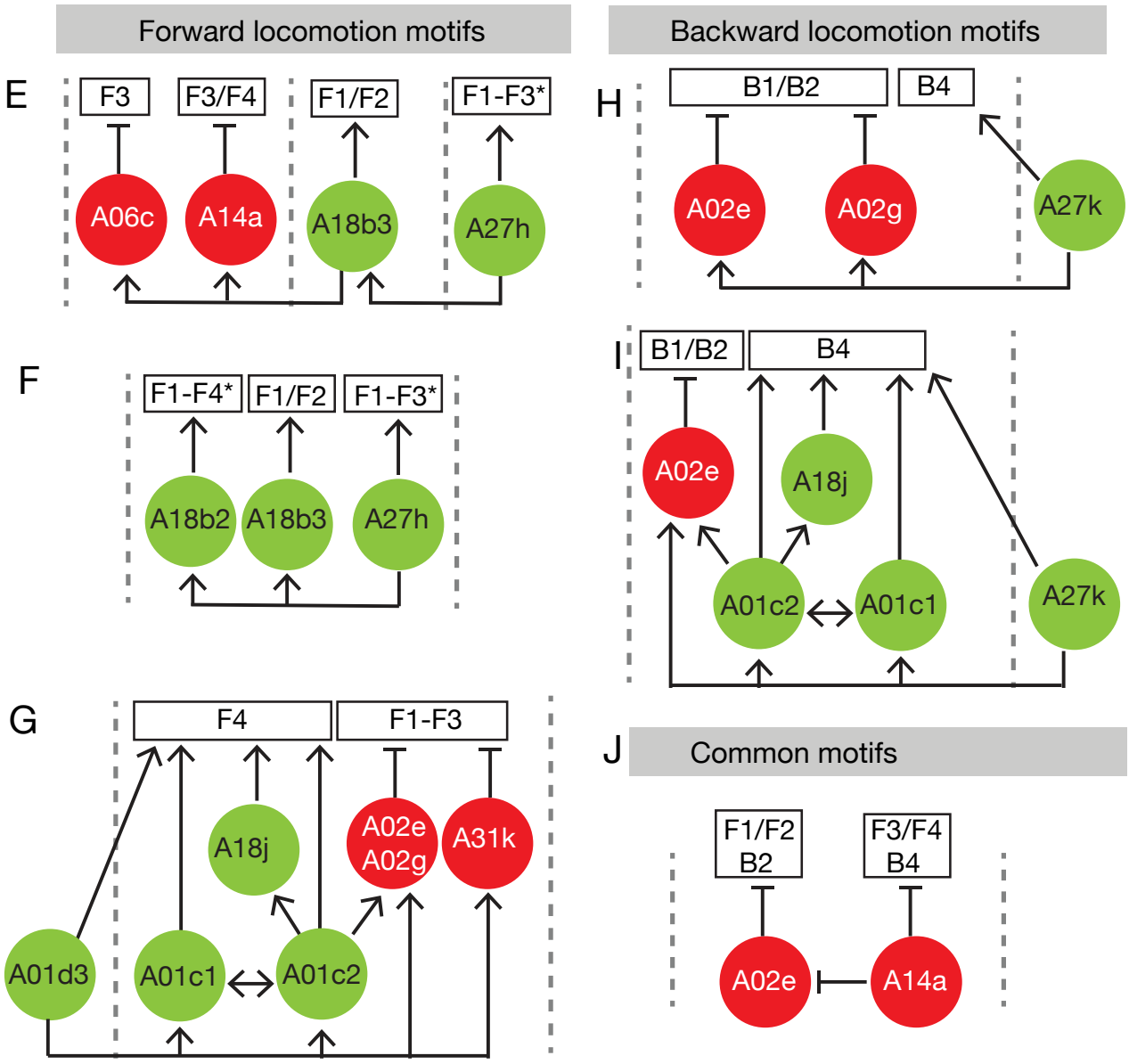

Figure 11

1034